Publication Year	2016
Acceptance in OA	2020-10-16T08:56:02Z
Title	Optical and near-infrared observations of SN 2014ck: an outlier among the Type Iax supernovae
Authors	TOMASELLA, Lina, CAPPELLARO, Enrico, BENETTI, Stefano, PASTORELLO, Andrea, Hsiao, E. Y., Sand, D. J., Stritzinger, M., Valenti, S., McCully, C., Arcavi, I., ELIAS DE LA ROSA, NANCY DEL CARMEN, Harmanen, J., Harutyunyan, A., Hosseinzadeh, G., Howell, D. A., Kankare, E., Morales-Garoffolo, A., Taddia, F., Tartaglia, L., Terreran, G., TURATTO, Massimo
Publisher's version (DOI)	10.1093/mnras/stw696
Handle	http://hdl.handle.net/20.500.12386/27854
Journal	MONTHLY NOTICES OF THE ROYAL ASTRONOMICAL SOCIETY
Volume	459

Monthly Notices of the ROYAL ASTRONOMICAL SOCIETY

MNRAS **459,** 1018–1038 (2016) doi:10.1093/mnras/stw696
Advance Access publication 2016 March 28

Optical and near-infrared observations of SN 2014ck: an outlier among the Type Iax supernovae

L. Tomasella,[1⋆] E. Cappellaro,[1] S. Benetti,[1] A. Pastorello,[1] E. Y. Hsiao,[2,3] D. J. Sand,[4] M. Stritzinger,[2] S. Valenti,[5,6] C. McCully,[5,6] I. Arcavi,[6,7] N. Elias-Rosa,[1] J. Harmanen,[8] A. Harutyunyan,[9] G. Hosseinzadeh,[5,6] D. A. Howell,[5,6] E. Kankare,[10] A. Morales-Garoffolo,[11] F. Taddia,[12] L. Tartaglia,[1] G. Terreran[1,10] and M. Turatto[1]

[1]*INAF, Osservatorio Astronomico di Padova, I-35122 Padova, Italy*
[2]*Department of Physics and Astronomy, Aarhus University, Ny Munkegade 120, DK-8000 Aarhus C, Denmark*
[3]*Department of Physics, Florida State University, 77 Chieftan Way, Tallahassee, FL 32306, USA*
[4]*Physics Department, Texas Tech University, Box 41051, Lubbock, TX 79409-1051, USA*
[5]*Department of Physics, University of California, Santa Barbara, Broida Hall, Mail Code 9530, Santa Barbara, CA 93106-9530, USA*
[6]*Las Cumbres Observatory Global Telescope Network, 6740 Cortona Dr, Suite 102, Goleta, CA 93117, USA*
[7]*Kavli Institute for Theoretical Physics, University of California, Santa Barbara, CA 93106, USA*
[8]*Tuorla Observatory, Department of Physics and Astronomy, University of Turku, Väisäläntie 20, FI-21500 Piikkiö, Finland*
[9]*Fundación Galileo Galilei, INAF Telescopio Nazionale Galileo, Rambla José Ana Fernández Pérez 7, E-38712 Breña Baja, TF, Spain*
[10]*Astrophysics Research Centre, School of Mathematics and Physics, Queen's University Belfast, Belfast BT7 1NN, UK*
[11]*Institut de Ciències de l'Espai (CSIC-IEEC), Campus UAB, Camí de Can Magrans S/N, E-08193 Cerdanyola (Barcelona), Spain*
[12]*Department of Astronomy, The Oskar Klein Centre, AlbaNova, SE-106 91 Stockholm, Sweden*

Accepted 2016 March 22. Received 2016 March 9; in original form 2015 November 30

ABSTRACT

We present a comprehensive set of optical and near-infrared (NIR) photometric and spectroscopic observations for SN 2014ck, extending from pre-maximum to six months later. These data indicate that SN 2014ck is photometrically nearly identical to SN 2002cx, which is the prototype of the class of peculiar transients named SNe Iax. Similar to SN 2002cx, SN 2014ck reached a peak brightness $M_B = -17.37 \pm 0.15$ mag, with a post-maximum decline rate $\Delta m_{15}(B) = 1.76 \pm 0.15$ mag. However, the spectroscopic sequence shows similarities with SN 2008ha, which was three magnitudes fainter and faster declining. In particular, SN 2014ck exhibits extremely low ejecta velocities, $\sim$3000 km s^{-1} at maximum, which are close to the value measured for SN 2008ha and half the value inferred for SN 2002cx. The bolometric light curve of SN 2014ck is consistent with the production of $0.10^{+0.04}_{-0.03}$ M$_\odot$ of ^{56}Ni. The spectral identification of several iron-peak features, in particular Co II lines in the NIR, provides a clear link to SNe Ia. Also, the detection of narrow Si, S and C features in the pre-maximum spectra suggests a thermonuclear explosion mechanism. The late-phase spectra show a complex overlap of both permitted and forbidden Fe, Ca and Co lines. The appearance of strong [Ca II] λλ7292, 7324 again mirrors the late-time spectra of SN 2008ha and SN 2002cx. The photometric resemblance to SN 2002cx and the spectral similarities to SN 2008ha highlight the peculiarity of SN 2014ck, and the complexity and heterogeneity of the SNe Iax class.

Key words: supernovae: general – supernovae: individual: SN 2014ck – supernovae: individual: SN 2006fp – galaxies: individual: UGC 12182.

1 INTRODUCTION

The discovery of several peculiar Type Ia supernovae (SNe Ia) has drawn the attention both to the photometric and spectroscopic diversity among this class of otherwise homogeneous transients. The dispersion of the luminosity–decline rate relation (Phillips 1993; Hamuy et al. 1995, 1996a) can be explained by an additional correlation between the decline rate and the colour at maximum light (Hamuy et al. 1996b; Branch 1998; Tripp 1998; Tripp & Branch 1999). Hence SNe Ia can be arranged into a photometric sequence extending from luminous, blue, slowly declining

⋆ E-mail: lina.tomasella@oapd.inaf.it

© 2016 The Authors
Published by Oxford University Press on behalf of the Royal Astronomical Society

Downloaded from https://academic.oup.com/mnras/article/459/1/1018/2609052 by CIS Psicologia Biblioteca F.Metelli - Universita degli Studi di Padova user on 30 September 2020

SN Ia, like SN 1991T, to normal events (Branch, Fisher & Nugent 1993), and finally to sub-luminous, red, quickly declining objects, like SN 1991bg (Filippenko et al. 1992a,b; Leibundgut et al. 1993; Turatto et al. 1996). SNe Ia also appear to form a spectroscopic sequence based on the systematic variations in the flux ratios of several spectral features near maximum light (e.g. Si II λλ5972, 6355; see Nugent et al. 1995). The common view is, despite their diversity, peculiar events such as the luminous 1991T-like and sub-luminous 1991bg-like SNe Ia, just like the normal population of SNe Ia, originate from the thermonuclear explosion of a C/O white dwarf (WD) that exceeds the Chandrasekhar mass after accreting mass from a companion star in a binary system.

However, there is a group of peculiar SNe Ia that challenges the canonical Chandrasekhar-mass explosion channel. The prototype of this class is SN 2002cx (Li et al. 2003), which shows a peak luminosity significantly lower than that of normal SNe Ia, even though its light-curve decline-rate parameter is comparable to normal events. Spectra obtained near maximum light resemble those of overluminous 1991T-like objects (with a blue continuum and absorption from higher ionization species), even if a low ejecta velocity ($\sim$6000 km s^{-1} at the epoch of B-band maximum light) points towards a moderate kinetic energy from the explosion (Li et al. 2003). The late-time spectra show narrow iron and cobalt lines (Li et al. 2003; Jha et al. 2006), in stark contrast to normal SNe Ia at similar epochs. After the pioneering studies by Li et al. (2003) and Jha et al. (2006) on SN 2002cx, both new and old SN discoveries have been classified or reclassified as 2002cx-like events, and it has become clear these transients are not so rare. This class was labelled Type Iax supernovae (SNe Iax) by Foley et al. (2013), who presented a review on the entire group and defined clear observational criteria to classify a Type Iax event.

A variety of explosion scenarios and potential progenitors or progenitor systems have been proposed to explain each event (see Liu et al. 2015b, and references therein for a recent review). Although the leading models for SNe Iax are thermonuclear explosion of a C/O WD (Foley et al. 2009; Jordan et al. 2012; Kromer et al. 2013; Fink et al. 2014; Kromer et al. 2015; Liu et al. 2015a; Stritzinger et al. 2015), a core-collapse scenario has been proposed at least for SN 2008ha (Foley et al. 2009; Valenti et al. 2009; Moriya et al. 2010), which is the most extreme member of SN Iax class to date. The latter however is controversial because of the detection of C/O burning products in the maximum-light spectrum of SN 2008ha (Foley et al. 2009, 2010b), providing a link to thermonuclear explosions. In principle, the best way to shed light on this issue would be the detection of a progenitor in pre-explosion images. Recently, McCully et al. (2014a) reported the detection of a luminous blue source coincident (at the 0.8σ level) with the location of Type Iax SN 2012Z in *Hubble Space Telescope* (*HST*) pre-explosion images. Although the photometric properties of this object suggest a C/O WD primary plus a He-star companion progenitor system, the explosion of a single massive star has not definitely been ruled out. In this case, post-explosion imaging, obtained after the SN fades away, should help to distinguish between the two models. For two other SNe Iax, no sources were detected in pre-explosion images, but limits were obtained that exclude massive stars as potential progenitors (SNe 2008ge and 2014dt; see Foley et al. 2010a, 2015).

Given the diversity of this SN class, one may consider the possibility that multiple progenitor channels may lead to the production of SNe Iax. In fact, the forty-some objects classified as SNe Iax have a number of similarities, but also noteworthy differences. In particular, they show a large range in luminosity at maximum, from $M_V \approx -14.2$ mag of the faint SN 2008ha (Foley et al. 2009; Valenti et al. 2009; Stritzinger et al. 2014) to $M_V \approx -18.5$ mag of SNe 2009ku (Narayan et al. 2011) and 2012Z (Stritzinger et al. 2015; Yamanaka et al. 2015). The ejecta velocities near maximum brightness also exhibit a large spread, ranging from $\sim$2000 to $\sim$8000 km s^{-1}. For the majority of SNe Iax, there appears to be a correlation between ejecta velocity and peak luminosity, with the higher velocity objects being also the brighter ones (McClelland et al. 2010; Foley et al. 2013). However, SN 2009ku, a low-velocity, high-luminosity SN studied by Narayan et al. (2011), does not follow the trend (note however that the first spectrum was taken long after maximum and so the inferred ejecta velocity is uncertain; see Foley et al. 2013). In this paper, we present the results of a comprehensive observational campaign of SN 2014ck, which started well before maximum light. It turns out that SN 2014ck is an outlier among SNe Iax, as it mirrors SN 2002cx from a photometric point of view, while the early spectra exhibit extremely narrow spectral lines, indicating very low expansion velocities of the ejecta.

This paper is organized as follows: in Section 2, we give some basic information about the SN discovery and the host galaxy, and we describe the follow-up campaign. In Section 3, we analyse *HST* pre-discovery images. We discuss data reduction and present the photometric evolution and visual and near-infrared (NIR) spectroscopic sequences of SN 2014ck in Section 4. In Section 5, the Galactic and host galaxy reddening is estimated. Descriptions of the photometric and spectroscopic properties of SN 2014ck are reported in Sections 6 and 7, respectively. Expansion velocities of the ejecta, along with the photospheric temperatures, are deduced from the spectra. Spectral modelling with the SYNOW code is used to assist in line identification. A final discussion of the available data in the context of the explosion models follows in Section 8.

2 SN 2014CK DISCOVERY AND FOLLOW-UP OBSERVATIONS

SN 2014ck was discovered by the Lick Observatory Supernova Search (LOSS; Filippenko et al. 2001), on 2014 June 29.47 UT, at an apparent magnitude of 16.4 mag using the Katzman Automatic Imaging Telescope (KAIT; Hayakawa et al. 2014). A marginal detection on 2014 June 24.5 UT was also reported by LOSS with an approximate R-band magnitude of 17.0 mag. However, a subsequent analysis of KAIT images on 2014 June 13, 23, 24, 25, 28 and 29, performed independently by the LOSS team (Zheng, private communication) and by us,[1] postpones this marginal detection by approximately one day (2014 June 25.5 UT, with an approximate r-band magnitude of 18.15 $\pm$ 0.44 mag, as reported in Table 6).

The SN is located 4.3 arcsec E and 0.5 arcsec S from the centre of the spiral galaxy UGC 12182 (Fig. 1). An heliocentric recessional velocity of 1490 km s^{-1} for UGC 12182 is listed in the NASA/IPAC Extragalactic Database (NED), as taken from 'The Updated Zwicky Catalogue' (Falco et al. 1999). The distance and distance modulus (adopting $H_0 = 73 \pm 5$ km s^{-1} Mpc^{-1}), corrected for the Virgo, Great Attractor and Shapley infall, are 24.4 $\pm$ 1.7 Mpc and $\mu = 31.94 \pm 0.15$ mag, respectively (Mould et al. 2000). We note that the correction for Virgo infall (see appendix A in Mould et al. 2000) includes two components: the correction for the infall to Virgo plus the vector contribution due to the Local Group's peculiar velocity with respect to Virgo. We also note that in the Local Group the radial peculiar velocity dispersion is estimated to be $\sim$60 km s^{-1}

[1] We thank WeiKang Zheng and Alex Filippenko for sending us LOSS/KAIT pre-discovery images.

Downloaded from https://academic.oup.com/mnras/article/459/1/1018/2609052 by CIS Psicologia Biblioteca F.Metelli - Universita degli Studi di Padova user on 30 September 2020

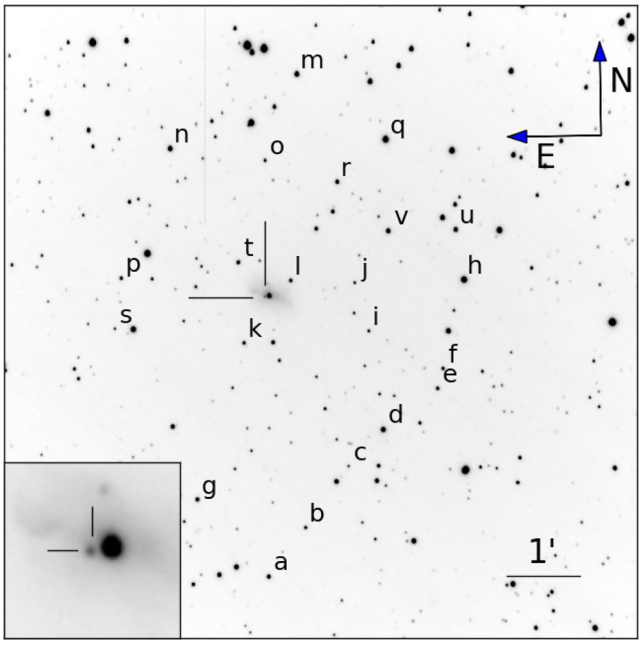

Figure 1. UGC 12182 and SN 2014ck: *r*-band image taken on 2014 October 28.84 UT with the Copernico 1.82 m Telescope (Asiago), with an inset of the SN region on the bottom left. The local sequence stars used for the calibration of non-photometric nights are indicated.

Table 1. Basic information on SN 2014ck and its host galaxy, UGC 12182.

Host galaxy	UGC 12182
Galaxy type	Sbc
Heliocentric radial velocity	$1490 \pm 19\,\mathrm{km\,s^{-1}}$
Distance modulus	31.94 ± 0.15 mag
Galactic extinction A_V	1.26 ± 0.15 mag
Total extinction A_V	$\approx 1.5 \pm 0.3$ mag
SN type	Iax
RA (J2000.0)	$22^{\mathrm{h}}45^{\mathrm{m}}38\overset{\mathrm{s}}{.}88$
Dec. (J2000.0)	$+73^{\circ}09'42\overset{''}{.}7$
Offset from nucleus	4.3 arcsec E, 0.5 arcsec S
Estimated date of explosion (MJD)	$56\,828.2^{+2.7}_{-4.5}$
Date of first detection (MJD)	56 832.5
Date of *V*-band maximum (MJD)	$56\,845.6 \pm 0.1$
M_V at maximum	-17.29 ± 0.15 mag
M_B at maximum	-17.37 ± 0.15 mag
L_{bol} at maximum	1.91×10^{42} erg s^{-1}

(see for example Feldman et al. 2003), which accounts for about 25 per cent of the total error budget on μ.

Soon after discovery, spectroscopic classifications of SN 2014ck were obtained independently at the Lick Observatory and under the Asiago Classification Program (Tomasella et al. 2014). The earliest spectrum indicated it was a SN Iax on the rise (Masi et al. 2014), resembling SN 2005hk (Phillips et al. 2007), SN 2008ha (Foley et al. 2009; Valenti et al. 2009) and SN 2010ae (Stritzinger et al. 2014).

Given the relatively small number of well-observed SNe Iax in the literature and the early detection and classification, we initiated a follow-up campaign aimed to collect detailed optical and NIR observations using several telescopes available to our collaboration.

Basic information of SN 2014ck and its host galaxy are summarized in Table 1. Following the discussion in Section 6, we adopt a *V*-band maximum estimate of MJD = 56845.6 ± 0.1, which we use as a reference epoch throughout this work.

3 *HST* PRE-EXPLOSION IMAGES

Another transient, SN 2006fp (Puckett et al. 2006) was previously discovered in the host galaxy of SN 2014ck. The nature of this transient is unclear, but it was likely an SN IIn or an SN impostor (i.e. the outburst of a luminous blue variable star), the latter being favoured by its spectral characteristics (Blondin et al. 2006).

HST imaging was obtained of the host of SN 2006fp with the Ultraviolet-Visible (UVIS) Channel of the Wide Field Camera 3 (WFC3) (pixel scale 0.04 arcsec pix^{-1}). Images were taken on 2013 February 22 UT (*HST* proposal ID 13029; PI: A. Filippenko) with the *F625W* (roughly *r*) and *F814W* (roughly *I*) passbands. The archival flat-fielded images (FLT) were retrieved from the *HST* MAST Archive[2] and re-reduced using the WFC3 UVIS CTE correction software[3] and the ASTRODRIZZLE software from the DRIZZLEPAC package (Gonzaga et al. 2012).

Next the absolute astrometry was registered to match the ground-based *g*-band images which were obtained with the LCOGT 2.0 m Telescope (Haleakala, Hawaii, USA) on 2014 August 11.37 UT. Astrometric alignment was accomplished by fitting a second-order Legendre polynomial with the IRAF[4] tasks GEOMAP and GEOXYTRAN, measuring the position of 16 stars that were visible in both the LCOGT and *HST* frames. This yielded an astrometric precision of 0.033 and 0.022 arcsec in the east–west and north–south directions, respectively.

The position of SN 2014ck in the LCOGT image was determined by fitting a Gaussian to the SN. We estimated the uncertainties in the position of the SN by running Markov chain Monte Carlo analysis using the EMCEE PYTHON package (Foreman-Mackey et al. 2013). We found that the uncertainty on the SN position was 50 mas.

Adding the astrometric solution and the positional uncertainties of the SN position in quadrature, we adopt a total uncertainty on the position in the *F625W* pre-explosion images to be 0.06 and 0.055 arcsec in the east–west and north–south directions, respectively (see Fig. 2).

We next used DOLPHOT[5] to measure the photometry of all the stars in the pre-explosion images. The sky subtraction (in this case, the sky subtraction includes the diffuse contribution from the host galaxy) and point spread function (PSF) fits were done using the recommended parameters from the DOLPHOT manual.

No source was detected within 3σ of the position of SN 2014ck. Using the detected sources from a 200 × 200 box centred around the SN position, we found 3σ limiting magnitudes of $m_{F625W} > 26.95$ and $m_{F814W} > 26.35$ mag in the Vega system. Adopting a distance modulus $\mu = 31.94$ mag and reddening estimate $E(B-V)_{\mathrm{tot}} \approx 0.5$ mag (see Section 5), we obtain absolute luminosity limits $m_{F625W} > -6.5$ mag. In passing, we note that there is no evidence of a stellar source at the position of SN 2006fp.

The search for progenitor candidates in pre-explosion *HST* images has previously been performed for the Type Iax SNe 2008ge

[2] https://archive.stsci.edu/hst/

[3] http://www.stsci.edu/hst/wfc3/

[4] IRAF is distributed by the National Optical Astronomy Observatory, which is operated by the Association of Universities for Research in Astronomy (AURA) under a cooperative agreement with the National Science Foundation.

[5] DOLPHOT is a stellar photometry package that was adapted from HSTPHOT (Dolphin 2000).

Downloaded from https://academic.oup.com/mnras/article/459/1/1018/2609052 by CIS Psicologia Biblioteca F.Metelli - Universita degli Studi di Padova user on 30 September 2020

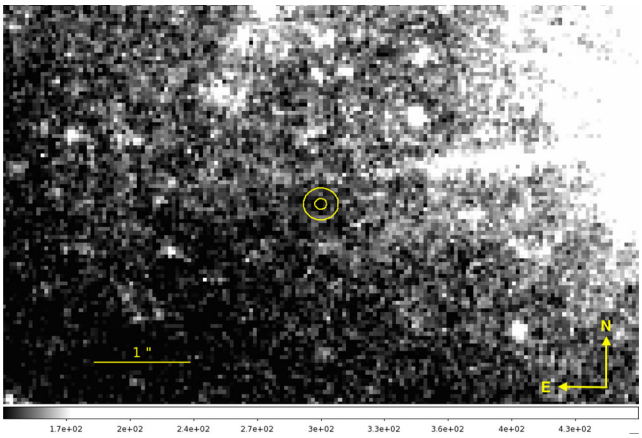

Figure 2. *HST* pre-explosion image (*F625W* filter). The position of SN 2014ck is marked with ellipses. The outer ellipse corresponds to three times the uncertainty in the SN position.

(Foley et al. 2010a), 2012Z (McCully et al. 2014a), and 2014dt (Foley et al. 2015). At position of SN 2012Z, McCully et al. (2014a) detected a bright ($M_{F435W} = -5.43 \pm 0.15$ mag, $m_{F814W} = -5.24 \pm 0.16$ mag, i.e. $M_V \sim -5.3$ mag) blue source, which they interpret as a non-degenerate He-star companion to a C/O WD. The source associated with SN 2012Z is the only probable progenitor system detected in pre-explosion images of SNe Iax and of any SN Ia (Li et al. 2011, and references therein). Wang et al. (2014) and Liu et al. (2015a,b) performed binary evolution simulations indicating this could indeed explain the observed photometry. Yet the possibility that the source associated with SN 2012Z is a massive star cannot be entirely ruled out. Planned observations after the fading of the SN may help to finally distinguish between these progenitor models (McCully et al. 2014a).

In the cases of SNe 2008ge and 2014dt, non-detections were reported and *HST* images were used by Foley et al. (2010a) and Foley et al. (2015) to place 3σ limits on the absolute magnitudes of the progenitors, corresponding to $M_V > -6.7$ mag and a relatively deep $M_{F450W} > -5.0$ mag, respectively. For SN 2014dt, Foley et al. (2015) excluded a massive star as the progenitor and suggested a C/O WD primary plus a He-star companion progenitor system, similar to SN 2012Z. For both SN 2008ge (Foley et al. 2010a) and SN 2014ck, the constraints on the luminosity of the undetected progenitor, a magnitude brighter than the SN 2012Z detection, rules out only the most-luminous Wolf–Rayet stars (roughly corresponding to stars with initial masses of 60–65 $M_\odot$; Crowther 2007).

4 OBSERVATION AND DATA REDUCTION

4.1 Photometry

Optical (*uBVgri*) and NIR (*JHK*) imaging of SN 2014ck started a few days after discovery and continued over the course of about six months. The telescopes and their associated instruments used for the photometric campaign are listed in Table 2.

All frames were pre-processed using standard procedures in IRAF for bias subtraction and flat fielding. For the NIR exposures, sky background subtraction was also performed. Multiple exposures obtained in the same night were aligned and combined to increase the signal-to-noise ratio.

Over the course of multiple photometric nights, Landolt (1992) and Sloan Digital Sky Survey (SDSS, Data Release 12, Alam et al. 2015)[6] standard fields were observed in order to calibrate a local sequence of stars in the field of UGC 12182 (see Table 3 and Fig. 1). The local sequence was used to compute zero-points for non-photometric nights. In the NIR, stars from the 2MASS catalogue were used for the calibration. We verified that photometry taken at similar phases but with different instrumentation were in excellent agreement with each other, checking, for all bands, the rms dispersion of the whole data set with respect to the dispersion of the sub-sets coming from each instrument. Thus no additional *S*-correction (Stritzinger et al. 2002) was applied.

All photometry was performed via PSF fitting using the SNOOPY package (Cappellaro 2014). SNOOPY is a collection of PYTHON scripts calling standard IRAF tasks (through PYRAF) and specific data analysis tools such as SExtractor for source extraction and DAOPHOT for PSF fitting. The sky background at the SN location is first estimated with a low-order polynomial fit to data in the surrounding area. Then, the PSF model derived from isolated field stars is simultaneously fitted to the SN and any point source projected nearby (i.e. any star-like source within a radius of $\sim 5 \times$ FWHM from the SN). The fitted sources are removed from the original images, an improved estimate of the local background is derived and the PSF fitting procedure iterated. The residuals are visually inspected to validate the fit.

An alternative approach for the measurement of transient magnitudes is template subtraction. The application of this technique requires the use of exposures of the field obtained before the SN explosion or after the SN has faded. The template images need to be in the same filter and have good signal to noise and seeing. Unfortunately, we could not find archival images suitable for use as templates, so only the PSF-fitting procedure was performed. On the contrary, for earlier epochs of LOSS/KAIT imaging, the pre-explosion image obtained on 2014 June 13 was used as a subtraction template (see Section 2).

Error estimates for the SN magnitudes are obtained through artificial star experiments in which a fake star with a similar magnitude to the SN is placed in the fit residual image at a position close to, but not coincident with, the SN location. The simulated image is processed through the same PSF fitting procedure and the standard deviation of magnitudes of the fake stars is taken as an estimate of the instrumental magnitude error, which is mainly due to the uncertainty in the background fitting. This is combined (in quadrature) with the PSF fit error returned by DAOPHOT and the propagated errors from the photometric calibration chain.

Johnson/Bessel and Sloan optical magnitudes of the SN and associated errors are listed in Tables 4 and 5, respectively, while the NIR photometry is given in Table 6. Magnitudes are in the Vega system for the Johnson/Bessel filters and are close to the AB system (SDSS = AB − 0.02 mag) for the Sloan filters.

The *uBVgriJHK* light curves of SN 2014ck are plotted in Fig. 3. Note that since only a handful of *RIz* epochs are available, we list their values in Tables 4 and 7 but do not plot them.

4.2 Spectroscopy

A sequence of 24 low-resolution visual-wavelength spectra for SN 2014ck were obtained extending from −6.0 d to +166.3 d relative to the epoch of *V*-band maximum. Seven epochs of NIR spectra were also taken extending from −1.0 d to +55 d. A summary of all spectroscopic observations is provided in Table 7.

[6] http://www.sdss.org

Downloaded from https://academic.oup.com/mnras/article/459/1/1018/2609052 by CIS Psicologia Biblioteca F.Metelli - Universita degli Studi di Padova user on 30 September 2020

Table 2. List of observing facilities employed for optical and NIR photometry.

Telescope[a]	Instrument	Site	FoV (arcmin^2)	Scale (arcsec pix^{-1})
		Optical facilities		
LCOGT	Spectral[b]	Haleakala, Hawaii (USA)	10 × 10	0.30
LCOGT	SBIG	McDonald Observatory, Texas (USA)	16 × 16	0.47
Copernico	AFOSC	Asiago, Mount Ekar (Italy)	8.8 × 8.8	0.48
NOT	ALFOSC	Roque de los Muchachos, La Palma, Canary Islands (Spain)	6.4 × 6.4	0.19
TNG	LRS	Roque de los Muchachos, La Palma, Canary Islands (Spain)	8.6 × 8.6	0.25
		NIR facilities		
NOT	NOTCam	Roque de los Muchachos, La Palma, Canary Islands (Spain)	4 × 4	0.23
TNG	NICS	Roque de los Muchachos, La Palma, Canary Islands (Spain)	4.2 × 4.2	0.25

Notes. [a]LCOGT = Las Cumbres Observatory Global Telescope Network (Brown et al. 2013); Copernico = INAF Osservatorio Astronomico di Padova 1.82 m Telescope (Mt. Ekar, Asiago, Italy); NOT = 2.56 m Nordic Optical Telescope (La Palma, Spain); TNG = 3.58m Telescopio Nazionale Galileo (La Palma, Spain).
[b]Spectral is a photometric camera mounted on the Faulkes Telelescopes of the LCOGT network.

Table 3. Magnitudes for the local sequence stars, as indicated in Fig. 1, with associated errors in parentheses (Vega mag).

ID	RA (J2000.0)	Dec. (J2000.0)	*U* (mag)	*B* (mag)	*V* (mag)	*R* (mag)	*I* (mag)
a	22:45:38.708	73:05:53.33	19.241 (0.024)	18.137 (0.016)	16.848 (0.023)	16.047 (0.019)	15.443 (0.013)
b	22:45:31.661	73:06:33.20	18.992 (0.026)	18.566 (0.015)	17.566 (0.019)	16.918 (0.006)	16.393 (0.013)
c	22:45:23.408	73:07:22.70	19.537 (0.019)	19.373 (0.008)	18.496 (0.016)	–	–
d	22:45:16.752	73:07:52.77	18.649 (0.002)	17.425 (0.008)	16.042 (0.015)	–	14.471 (0.006)
e	22:45:06.405	73:08:25.75	18.402 (0.006)	18.189 (0.002)	17.295 (0.008)	16.646 (0.002)	16.119 (0.014)
f	22:45:05.321	73:08:42.04	18.833 (0.028)	18.526 (0.003)	17.568 (0.012)	16.867 (0.004)	16.325 (0.022)
g	22:45:51.990	73:06:56.89	17.739 (0.024)	17.501 (0.012)	16.631 (0.013)	16.078 (0.004)	15.570 (0.010)
h	22:45:01.180	73:09:54.94	18.027 (0.010)	16.653 (0.004)	15.310 (0.016)	14.397 (0.021)	13.565 (0.027)
i	22:45:19.245	73:09:13.70	19.239 (0.008)	18.956 (0.010)	17.986 (0.011)	17.408 (0.028)	16.747 (0.008)
j	22:45:21.834	73:09:53.57	19.537 (0.008)	19.171 (0.012)	18.166 (0.014)	17.636 (0.018)	16.975 (0.008)
k	22:45:42.885	73:09:05.03	18.547 (0.019)	18.216 (0.008)	17.381 (0.010)	16.928 (0.014)	16.365 (0.012)
l	22:45:33.912	73:09:55.99	19.115 (0.005)	18.457 (0.010)	17.398 (0.006)	16.804 (0.011)	16.144 (0.016)
m	22:45:32.298	73:12:45.27	18.003 (0.002)	17.157 (0.005)	15.966 (0.017)	15.329 (0.012	14.566 (0.006)
n	22:45:56.437	73:11:45.34	17.787 (0.017)	17.024 (0.009)	15.908 (0.010)	15.322 (0.014)	14.613 (0.013)
o	22:45:38.507	73:11:34.89	18.715 (0.008)	18.475 (0.002)	17.628 (0.026)	17.171 (0.006)	16.534 (0.002)
p	22:46:05.921	73:09:59.35	18.456 (0.005)	18.117 (0.005)	17.233 (0.019)	16.754 (0.012)	16.144 (0.008)
q	22:45:15.643	73:11:50.85	15.884 (0.008)	15.661 (0.011)	14.865 (0.012)	14.406 (0.014)	13.813 (0.016)
r	22:45:24.907	73:11:16.49	17.944 (0.017)	17.647 (0.011)	16.715 (0.012)	16.195 (0.005)	15.529 (0.016)
s	22:46:07.248	73:09:17.79	19.529 (0.001)	19.220 (0.009)	18.343 (0.011)	17.887 (0.017)	17.313 (0.009)
t	22:45:43.815	73:10:11.37	18.262 (0.002)	17.925 (0.013)	17.024 (0.018)	–	–
u	22:45:02.577	73:10:36.09	17.689 (0.003)	17.329 (0.007)	16.410 (0.005)	15.770 (0.005)	15.171 (0.027)
v	22:45:15.320	73:10:35.72	17.378 (0.000)	17.130 (0.005)	16.199 (0.002)	15.660 (0.004)	15.066 (0.013)

Optical spectra were reduced using standard IRAF tasks. After bias and flat-field correction, the SN spectrum was extracted and calibrated in wavelength through a comparison to arc lamp spectra. The flux calibration was derived from observations of spectrophotometric standard stars obtained, when possible, on the same night as the SN. All the flux-calibrated spectra were verified against photometry and, when necessary, a correction factor was applied. Corrections for the telluric absorption bands were derived using the spectrophotometric standard star spectra. In some cases, a non-perfect removal can affect the SN features that overlap with the strongest atmospheric absorptions, in particular with the telluric O_2 *A* band at 7590–7650 Å and the H_2O, CO_2, CH_4 bands in NIR spectra (their positions are marked in Figs 8, 9, 10, 11, 13, 14 and 15 with the ⊕ symbol and, for the strongest ones, with vertical grey bands).

The NIR spectra obtained with GNIRS attached to the Gemini North telescope were reduced using the GNIRS Gemini IRAF package (see Hsiao et al. 2013, for details). The TNG spectrum obtained with the Near Infrared Camera Spectrograph (NICS) was reduced using standard IRAF packages. In brief, following the standard infrared technique, each night several pairs of spectra were taken at different positions along the slit, and consecutive pairs were subtracted from each other in order to remove the sky background. The subtracted images were aligned to match the stellar profile and added together. Finally, the source spectrum was extracted from the combined images. Wavelength calibration, telluric correction and flux calibration were done in the standard manner. Lastly, spectra were corrected to match the broad-band photometry.

5 GALACTIC AND HOST REDDENING

The Galactic extinction in the direction of UGC 12182, as derived from the Schlafly & Finkbeiner (2011) recalibration of the Schlegel, Finkbeiner & Davis (1998) infrared-based dust map, is $E(B-V)_G = 0.40 \pm 0.05$ mag (via NED), which corresponds to a Galactic extinction $A_V = 1.26 \pm 0.15$ mag when adopting a standard $R_V = 3.1$ reddening law (Cardelli, Clayton & Mathis 1989).

Downloaded from https://academic.oup.com/mnras/article/459/1/1018/2609052 by CIS Psicologia Biblioteca F.Metelli - Universita degli Studi di Padova user on 30 September 2020

Table 4. Optical photometry of SN 2014ck in the Johnson/Cousins *UBVRI* filters (Vega mag), with associated errors in parentheses.

Date	MJD	*U* (mag)	*B* (mag)	*V* (mag)	*R* (mag)	*I* (mag)	Instrument
20140630	56838.83	–	–	–	16.1 (0.5)	–	Masi[a]
20140701	56839.38	–	–	17.34 (0.23)	–	–	Brimacombe[a,b]
20140701	56839.91	–	–	–	16.1 (0.5)	–	James[a]
20140704	56842.01	–	–	16.64 (0.22)	–	–	AFOSC
20140705	56843.57	–	–	16.49 (0.20)	–	–	Spectral[c]
20140706	56844.42	–	16.89 (0.06)	16.44 (0.04)	–	–	SBIG
20140706	56844.60	–	–	16.44 (0.22)	–	–	Spectral[c]
20140708	56846.30	–	16.91 (0.03)	16.43 (0.03)	–	–	SBIG
20140711	56849.10	–	17.22 (0.02)	16.53 (0.01)	–	–	LRS
20140716	56854.44	–	18.11 (0.04)	16.85 (0.03)	–	–	Spectral[c]
20140719	56857.07	–	18.35 (0.05)	17.20 (0.07)	–	–	AFOSC
20140724	56862.58	–	–	17.31 (0.15)	–	–	Spectral[c]
20140725	56863.45	–	18.97 (0.04)	17.47 (0.04)	–	–	Spectral[c]
20140726	56864.31	–	–	17.49 (0.39)	–	–	SBIG
20140728	56866.49	–	–	17.62 (0.17)	–	–	Spectral[c]
20140731	56869.54	–	19.35 (0.05)	17.76 (0.04)	–	–	Spectral[c]
20140803	56872.97	–	19.29 (0.06)	17.72 (0.03)	–	–	AFOSC
20140805	56874.13	20.18 (0.06)	19.45 (0.02)	17.91 (0.01)	17.27 (0.08)	16.64 (0.01)	ALFOSC
20140812	56881.36	–	–	18.19 (0.23)	–	–	Spectral[c]
20140813	56882.01	–	19.69 (0.03)	18.16 (0.02)	–	–	LRS
20140816	56885.36	–	–	18.29 (0.18)	–	–	Spectral[c]
20140820	56889.46	–	19.69 (0.15)	18.29 (0.03)	–	–	Spectral[c]
20140824	56893.42	–	19.82 (0.14)	18.40 (0.03)	–	–	Spectral[c]
20140824	56893.97	20.95 (0.07)	19.84 (0.02)	18.45 (0.03)	17.80 (0.02)	17.16 (0.02)	ALFOSC
20140825	56894.36	–	19.67 (0.06)	18.43 (0.04)	–	–	Spectral[c]
20140825	56894.44	–	–	18.53 (0.21)	–	–	SBIG
20140829	56898.36	–	19.92 (0.15)	18.52 (0.04)	–	–	Spectral[c]
20140829	56898.47	–	–	18.56 (0.20)	–	–	SBIG
20140902	56902.26	–	19.84 (0.13)	18.58 (0.04)	–	–	SBIG
20140902	56902.53	–	19.84 (0.05)	18.58 (0.04)	–	–	Spectral[c]
20140906	56906.32	–	19.99 (0.07)	18.59 (0.05)	–	–	Spectral[c]
20140909	56909.44	–	–	18.67 (0.09)	–	–	SBIG
20140910	56910.30	–	19.89 (0.10)	18.74 (0.05)	–	–	Spectral[c]
20140914	56914.44	–	20.17 (0.07)	18.79 (0.04)	–	–	Spectral[c]
20140918	56918.50	–	20.06 (0.05)	18.87 (0.03)	–	–	SBIG
20140922	56922.39	–	20.13 (0.04)	18.93 (0.04)	–	–	Spectral[c]
20140923	56923.39	–	–	19.00 (0.04)	–	–	Spectral[c]
20140927	56927.03	–	20.11 (0.18)	18.95 (0.21)	–	–	AFOSC
20140928	56928.32	–	20.21 (0.18)	19.03 (0.11)	–	–	Spectral[c]
20141013	56943.83	21.94 (0.18)	20.58 (0.03)	19.32 (0.02)	18.86 (0.06)	18.04 (0.02)	ALFOSC
20141024	56954.83	–	20.47 (0.19)	19.34 (0.21)	–	–	AFOSC
20141028	56958.82	–	20.58 (0.21)	19.41 (0.21)	–	–	AFOSC
20141125	56986.82	–	20.93 (0.07)	19.93 (0.10)	19.30 (0.10)	18.68 (0.15)	ALFOSC
20141216	57007.85	–	21.71 (0.08)	20.34 (0.05)	19.89 (0.06)	18.76 (0.05)	ALFOSC
20150110	57032.75	–	22.41 (0.52)	21.52 (0.56)	–	–	AFOSC

Notes. [a]From IAU CBET 3949 (Masi et al. 2014); [b]*V* for reference; [c]'Spectral' is a photometric camera mounted on the Faulkes Telescopes of the LCOGT network.

The extinction within the host galaxy is more uncertain. A standard approach for SNe Ia is to measure the colour excess by comparing the SN colour with that of an unreddened SN template. However, the comparative study of the $B - V$, $V - R$ and $V - I$ colour curves for a sample of SNe Iax presented by Foley et al. (2013) shows significant scatter that does not improve after reddening corrections. So far, it is unclear if these objects have similar intrinsic colours or not. High-dispersion observations of Na I D λλ5890, 5896 are used as an independent means of probing dust extinction to extragalactic sources (Poznanski, Prochaska & Bloom 2012). However, for medium- to low-resolution spectra, when the doublet is blended, there is a large scatter in the data (Turatto, Benetti & Cappellaro 2003; Poznanski et al. 2011) and the correlation has less predictive power. Moreover, Phillips et al. (2013) showed that the column density and/or equivalent width (EW) of the Na I D lines are, in general, unreliable indicators of the extragalactic dust extinction suffered by SNe Ia. The exception to this statement is that weak or undetectable Na I absorption appears to be consistent with little or no extinction. With this caveat in mind, the earlier spectra with the highest signal-to-noise ratio were selected from our spectral sequence and used to measure an average EW for the Galactic Na I D of 2.8 ± 0.3 Å. Following Turatto et al.

Downloaded from https://academic.oup.com/mnras/article/459/1/1018/2609052 by CIS Psicologia Biblioteca F.Metelli - Universita degli Studi di Padova user on 30 September 2020

Table 5. Optical photometry of SN 2014ck in the Sloan *ugriz* filters (AB mag), with associated errors in parentheses.

Date	MJD	*u* (mag)	*g* (mag)	*r* (mag)	*i* (mag)	*z* (mag)	Instrument
20140624	56832.46	–	–	18.41 (2.00)	–	–	KAIT[a,b]
20140625	56833.49	–	–	18.15 (0.44)	–	–	KAIT[a,c]
20140628	56836.49	–	–	16.96 (0.36)	–	–	KAIT[a]
20140629	56837.47	–	–	16.89 (0.11)	–	–	KAIT[a]
20140630	56838.41	–	–	16.71 (0.27)	–	–	KAIT[a]
20140704	56842.01	–	–	16.37 (0.02)	16.32 (0.02)	–	AFOSC
20140705	56843.57	–	–	16.32 (0.05)	16.19 (0.06)	–	Spectral[d]
20140706	56844.61	–	16.73 (0.10)	16.20 (0.08)	16.09 (0.11)	–	Spectral[d]
20140708	56846.32	–	16.70 (0.06)	16.19 (0.04)	16.14 (0.05)	–	SBIG
20140711	56849.18	18.35 (0.02)	16.81 (0.09)	16.28 (0.03)	16.06 (0.01)	–	LRS
20140713	56851.53	–	–	16.27 (0.03)	16.18 (0.04)	–	Spectral[d]
20140716	56854.44	–	17.67 (0.04)	16.48 (0.06)	16.24 (0.05)	–	Spectral[d]
20140719	56857.07	20.20 (0.14)	17.85 (0.03)	16.60 (0.04)	16.10 (0.03)	17.70 (0.06)	AFOSC
20140724	56862.58	–	18.27 (0.05)	16.83 (0.09)	16.51 (0.11)	–	Spectral[d]
20140725	56863.46	–	18.49 (0.06)	16.89 (0.04)	16.59 (0.08)	–	Spectral[d]
20140726	56864.32	–	18.50 (0.07)	16.95 (0.06)	16.64 (0.07)	–	SBIG
20140728	56866.50	–	18.57 (0.06)	17.08 (0.05)	16.70 (0.08)	–	Spectral[d]
20140731	56869.54	–	18.78 (0.05)	17.26 (0.06)	16.86 (0.09)	–	Spectral[d]
20140803	56872.97	21.08 (0.19)	18.72 (0.04)	17.34 (0.02)	17.01 (0.02)	–	AFOSC
20140805	56874.13	21.03 (0.06)	–	–	–	–	ALFOSC[e]
20140812	56881.38	–	19.13 (0.08)	17.67 (0.05)	17.37 (0.07)	–	Spectral[d]
20140813	56882.01	21.46 (0.21)	19.10 (0.09)	17.75 (0.11)	17.34 (0.13)	–	LRS
20140816	56885.36	–	19.19 (0.04)	17.79 (0.06)	17.39 (0.07)	–	Spectral[d]
20140820	56889.47	–	19.18 (0.05)	17.93 (0.05)	17.53 (0.08)	–	Spectral[d]
20140824	56893.43	–	–	–	17.52 (0.34)	–	Spectral[d]
20140824	56893.97	21.81 (0.07)	–	–	–	–	ALFOSC[e]
20140825	56894.36	–	19.27 (0.06)	18.07 (0.05)	17.75 (0.08)	–	Spectral[d]
20140825	56894.46	–	19.26 (0.11)	18.06 (0.07)	17.82 (0.07)	–	SBIG
20140829	56898.38	–	–	18.08 (0.17)	17.69 (0.08)	–	Spectral[d]
20140829	56898.45	–	19.32 (0.07)	18.21 (0.06)	17.82 (0.09)	–	SBIG
20140902	56902.45	–	19.49 (0.11)	18.23 (0.06)	17.85 (0.08)	–	SBIG
20140902	56902.54	–	19.34 (0.07)	18.25 (0.07)	17.91 (0.08)	–	Spectral[d]
20140906	56906.33	–	–	18.32 (0.06)	17.96 (0.10)	–	Spectral[d]
20140909	56909.42	–	19.37 (0.15)	18.36 (0.08)	17.95 (0.20)	–	SBIG
20140910	56910.32	–	19.42 (0.06)	18.44 (0.07)	18.06 (0.04)	–	Spectral[d]
20140914	56914.46	–	19.52 (0.07)	18.53 (0.05)	18.18 (0.10)	–	Spectral[d]
20140918	56918.51	–	19.54 (0.07)	18.55 (0.06)	18.14 (0.10)	–	Spectral[d]
20140922	56922.40	–	19.68 (0.07)	18.70 (0.08)	–	–	Spectral[d]
20140923	56923.40	–	19.70 (0.07)	18.64 (0.16)	18.31 (0.17)	–	Spectral[d]
20140927	56927.04	–	19.67 (0.19)	18.77 (0.17)	18.30 (0.04)	19.33 (0.13)	AFOSC
20141013	56943.83	22.79 (0.18)	–	–	–	–	ALFOSC[e]
20141024	56954.83	–	19.87 (0.17)	19.32 (0.19)	18.80 (0.18)	–	AFOSC
20141028	56958.83	–	20.03 (0.10)	19.42 (0.10)	18.93 (0.08)	–	AFOSC
20150110	57032.77	–	22.80 (0.36)	22.07 (0.45)	21.64 (0.47)	–	AFOSC

Notes. [a]LOSS/KAIT unfiltered images calibrated to *r*-band; [b]upper limit; [c]marginal detection; [d]'Spectral' is a photometric camera mounted on the Faulkes Telescopes of the LCOGT network; [e]*U*-band magnitude converted into *u* band following Chonis & Gaskell (2008).

Table 6. NIR photometry of SN 2014ck, with associated errors in parentheses.

Date	MJD	*J* (mag)	*H* (mag)	*K* (mag)	Instrument
20140807	56876.08	16.94 (0.03)	16.30 (0.01)	16.39 (0.03)	NOTCam
20140831	56900.08	17.58 (0.29)	16.59 (0.17)	16.91 (0.26)	NICS
20140905	56905.03	17.70 (0.03)	16.67 (0.05)	17.08 (0.05)	NOTCam
20141007	56937.07	18.16 (0.04)	17.39 (0.07)	17.75 (0.05)	NOTCam
20150105	57027.83	18.89 (0.04)	18.55 (0.09)	19.34 (0.26)	NOTCam

(2003), a lower limit for the colour excess within the Milky Way of $E(B-V)_{\rm G} = 0.44 \pm 0.05$ mag was found, in fair agreement with $E(B-V)_{\rm G} = 0.40 \pm 0.05$ mag obtained from the infrared maps of the galactic dust distribution. Only a weak absorption line, EW $\lesssim 0.3$ Å, may be attributed to the host Na I D. This is consistent with little extinction in the host galaxy ($E(B-V)_{\rm host} \lesssim 0.05$ mag). Therefore, the total colour excess of the SN is estimated to be $E(B-V)_{\rm tot} \approx 0.5 \pm 0.1$ mag (i.e. $A_V \approx 1.5 \pm 0.3$ mag).

Downloaded from https://academic.oup.com/mnras/article/459/1/1018/2609052 by CIS Psicologia Biblioteca F.Metelli - Universita degli Studi di Padova user on 30 September 2020

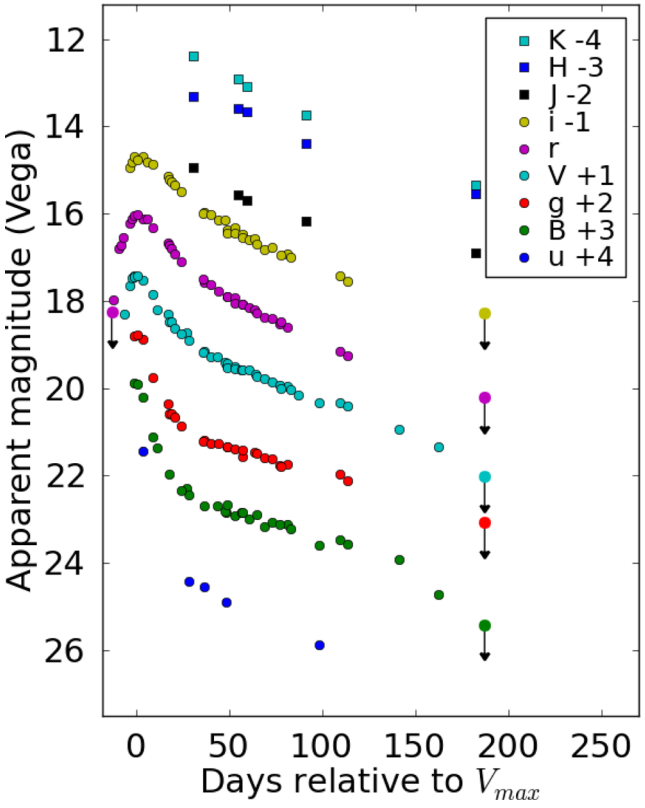

Figure 3. Light curves of SN 2014ck in the *uBVgriJHK* bands. Sloan *ugri* AB magnitudes have been here plotted as Vega magnitudes for uniformity with *BVJHK* bands, following Blanton & Roweis (2007). For clarity, the light curves have been shifted vertically as indicated in the legend. The uncertainties for most data points are smaller than the plotted symbols. The last *BVgri* photometric epoch is an upper limit.

6 PHOTOMETRIC EVOLUTION

6.1 Broad-band photometry

The photometric evolution of SN 2014ck shown in Fig. 3 is well sampled in the optical bands (except the pre-maximum evolution in *u* and *B* bands), while only a handful of NIR measurements were obtained. The light curves are characterized by a rise to maximum and a subsequent decline that is slower at longer wavelengths (e.g. in the *r* and *i* bands). Moreover, as already noted for other SNe Iax (Li et al. 2003; Foley et al. 2013; Stritzinger et al. 2015), the NIR bands show no evidence of a secondary maximum, characteristic of normal SNe Ia (Hamuy et al. 1996a,b). By using of a low-order polynomial fit to the optical light curves around maximum, an estimate of the magnitude and epoch of maximum light for each band was obtained. SN 2014ck reached peak brightness $M_B = -17.37 \pm 0.15$ mag and $M_V = -17.29 \pm 0.15$ mag. All the absolute magnitudes are listed in Table 8 along with their associated uncertainties estimated from the dispersion around the polynomial fit. Whereas the *gVri* light curves are well sampled around maximum, the *B*-band light curve is already declining from the first *B* point. Consequently, the time of *B*-band maximum might be ill constrained.

With best-fitting peak apparent magnitudes in hand, absolute magnitudes were also computed, with associated uncertainties obtained by adding in quadrature the errors of the fit to the peak apparent magnitudes and the errors in the adopted extinction and distance.

Finally, our polynomial fits also provide a measure of the decline-rate parameter Δm_{15}, the magnitude drop from the epoch of maximum brightness to 15 d later. In the case of normal SNe Ia, Δm_{15} is known to correlate with luminosity (Phillips 1993).

Examining the results of the polynomial fits, we find that maximum light is reached earlier in the blue bands compared to the red bands, with a delay of ∼4 d between the epochs of *B*- and *i*-band maximum. Furthermore, the blue bands have faster decline rates, with $\Delta m_{15}(B) = 1.76 \pm 0.15$ mag and $\Delta m_{15}(i) = 0.39 \pm 0.15$ mag. Both of these characteristics are common to all SNe Iax (Foley et al. 2013; Stritzinger et al. 2014, 2015).

As revealed from the comparison in Fig. 4 of the *B*- and *V*-band light curves of SN 2002cx and SN 2014ck, the two objects show nearly identical evolution. Moreover, as shown in Fig. 7, the two objects reached the same peak bolometric luminosity. The decline rates of the two objects are also nearly identical: $\Delta m_{15}(B) = 1.76 \pm 0.15$ mag for SN 2014ck versus $\Delta m_{15}(B) = 1.7 \pm 0.1$ mag for SN 2002cx. These values are significantly slower than the decline rate of the faint and fast SN 2008ha (Valenti et al. 2009, $\Delta m_{15}(B) = 2.03 \pm 0.20$ mag) and SN 2010ae (Stritzinger et al. 2014, $\Delta m_{15}(B) = 2.43 \pm 0.11$ mag). In conclusion, SN 2014ck follows the general trend for SNe Iax (and SNe Ia, in general): more luminous objects tend to have broader light curves (Foley et al. 2013).

Various optical-band colour curves of SN 2014ck, corrected for reddening, are plotted in Fig. 5. At early phases, the colours are blue. As the SN evolves, the colours change towards the red, reaching a maximum value around three weeks past maximum. Subsequently, the colours slowly evolve back towards the blue. Inspecting the colour curves of SN 2014ck compared to those of the Type Iax SN 2002cx (Li et al. 2003) and SN 2005hk (Phillips et al. 2007; Stritzinger et al. 2015), we note similar evolution, with SN 2014ck appearing marginally bluer over all epochs.

6.2 Explosion date and rise time estimates

The early detection of SN 2014ck and the analysis of LOSS/KAIT pre-discovery and discovery images gives a unique opportunity to obtain an accurate estimate of the rise time for an SN Iax. In order to constrain the explosion date of SN 2014ck, we fit the pre-maximum portion of the *r*- and *V*-band light curves (five epochs for each band) with an 'expanding fireball' model, i.e. $f_{\rm model}(t) = \alpha(t - t_0)^n$ with $n = 2$ (Riess et al. 1999, and references therein). The time of the first light (t_0) obtained from the fit (see Fig. 6) is MJD $= 56828.2^{+2.7}_{-4.5}$ (2014 June 20.2 UT). With regards to the index of the power law *n*, Firth et al. (2015) presented an analysis of the early, rising light curves for a sample of 18 SNe Ia: their data highlighted in many cases a departure of *n* from the simple fireball model ($n = 2$), with significant diversity from event to event (cf. their table 4 and fig. 14) and a mean value of the distribution of $n = 2.44 \pm 0.13$. Ganeshalingam, Li & Filippenko (2011), using a sample of about 60 low-redshift LOSS SNe Ia, found a best fit of $n = 2.20^{+0.27}_{-0.19}$, consistent (1σ) with the expanding fireball modelled by a parabola. In any case, these recent studies provide evidence for a range of *n* for SNe Ia events with the centre of the distribution slightly above 2 (see also Piro & Nakar 2014). This deviation has implications for the distribution of ^{56}Ni throughout the SN ejecta and so, in principle, the fit of the light curves should be *n* free. Unfortunately, pre-maximum data for SN 2014ck are not enough for a convergent solution with a free *n* parameter. To account for possible deviations from the fireball model, we fit a range of power laws with $2 \leq n \leq 2.5$ to the pre-maximum *r*- and *V*-band light curves independently. The reported uncertainty on t_0 is the standard deviation of the t_0

Downloaded from https://academic.oup.com/mnras/article/459/1/1018/2609052 by CIS Psicologia Biblioteca F.Metelli - Universita degli Studi di Padova user on 30 September 2020

Table 7. Journal of spectroscopic observations.

Date	MJD	Phase[a] (d)	Instrumental configuration[b]	Range (Å)	Resolution[c] (Å)
20140701	56839.58	−6.0	LCOGT+FLOYDS	3200–10 000	13
20140702	56840.52	−5.0	LCOGT+FLOYDS	3200–10 000	13
20140703	56841.52	−4.0	LCOGT+FLOYDS	3200–10 000	13
20140703	56841.98	−3.6	Ekar+AFOSC+gm4	3500–8200	24
20140704	56842.57	−3.0	LCOGT+FLOYDS	3200–10 000	13
20140706	56844.52	−1.0	LCOGT+FLOYDS	3200–10 000	13
20140706	56844.55	−1.0	Gemini-N+GNIRS	9800–25 000	4
20140707	56845.50	− 0.1	Gemini-N+GNIRS	9800–25 000	4
20140709	56847.21	1.7	NOT+ALFOSC+gm4	3400–9000	14
20140710	56848.49	2.9	LCOGT+FLOYDS	3200–10 000	13
20140711	56849.19	3.6	TNG+LRS+LR-B	3200–8000	10
20140711	56849.45	3.9	Gemini-N+GNIRS	9800–25 000	4
20140712	56850.58	5.0	LCOGT+FLOYDS	3200–10 000	13
20140718	56856.99	11.4	Ekar+AFOSC+gm4+VPH6	3500–9300	24
20140724	56862.20	16.6	NOT+ALFOSC+gm4	3400–9000	14
20140725	56863.58	18.0	LCOGT+FLOYDS	3200–10 000	13
20140726	56864.51	19.0	Gemini-N+GNIRS	9800–25 000	4
20140727	56865.56	20.0	LCOGT+FLOYDS	3200–10 000	13
20140728	56866.54	21.0	LCOGT+FLOYDS	3200–10 000	13
20140731	56869.28	23.7	Gemini-N+GNIRS	9800–25 000	4
20140801	56870.18	24.6	NOT+ALFOSC+gm4	3400–9000	14
20140805	56874.50	28.9	LCOGT+FLOYDS	3200–10 000	13
20140807	56876.39	30.8	Gemini-N+GNIRS	9800–25 000	4
20140812	56881.98	36.4	TNG+LRS+LR-B+LR-R	3500–10 000	10
20140815	56884.54	39.0	LCOGT+FLOYDS	3200–10 000	13
20140823	56892.36	46.8	LCOGT+FLOYDS	3200–10 000	13
20140825	56894.00	48.4	NOT+ALFOSC+gm4	3400–9000	14
20140831	56900.94	55.4	TNG+NICS+IJ+HK	9000–17 500	6
20140926	56926.94	81.4	Ekar+AFOSC+gm4+VPH6	3500–9300	24
20141025	56955.94	110.4	TNG+LRS+LR-B+LR-R	3500–10 000	10
20141220	57011.89	166.3	GTC+OSIRIS+R300B	3500–9000	16

Notes. [a]The phase is relative to the adopted epoch of the *V*-band maximum, MJD = 56845.6 ± 0.1.
[b]NOT = 2.56 m Nordic Optical Telescope (La Palma, Spain); Ekar = Copernico 1.82 m Telescope (Mt. Ekar, Asiago, Italy); TNG = 3.58 m Telescopio Nazionale Galileo (La Palma, Spain); LCOGT = LCOGT 2.0 m Telescope (Haleakala, Hawaii, USA); Gemini-N = 8.1 m Telescope (Hilo, Hawaii, USA); GTC = 10.4 m Gran Telescopio Canarias (La Palma, Spain).
[c]The resolution is estimated from the FWHM of the night sky lines.

parameters for these fits. We note that the spectral phases obtained by comparing the early spectra of SN 2014ck with similar-phase spectra of SN 2005hk are consistent with this estimate.

The rise time to maximum is estimated to range from ∼17 d in the *B* band to ∼21 d in the *i* band. The *BVgri*-band rise time estimates are listed in Table 8. The associated errors are largely dominated by the error on t_0. From the bolometric luminosity (see Section 6.3), we infer a rise time of $t_{\rm rise} = 16.9^{+4.5}_{-2.7}$ d, in agreement with the *B*-band rise time. This is not surprising, as the *B* band roughly traces the bolometric behaviour (Ganeshalingam et al. 2011). Note the rise times for SNe Iax range from SN 2008ha, at ∼10 d, to SN 2008ge, which might be >20 d (Foley et al. 2013).

6.3 Bolometric light curve and explosion parameter estimates

Using the multiband photometry of SN 2014ck extending from *u* to *K* bands, we constructed the pseudo-bolometric optical-infrared (OIR) light curve shown in Fig. 7. Unfortunately, no ultraviolet observations of SN 2014ck are available to compute a UVOIR bolometric light curve.[7]

For each epoch and passband, the observed magnitude was converted to flux at the effective wavelength. If observations were not available for a given filter on a particular night, the magnitude was estimated through interpolation between adjacent epochs or, if necessary, extrapolated assuming a constant colour from the closest available epoch. The fluxes were next corrected for reddening ($E(B-V)_{\rm tot} \approx 0.5 \pm 0.1$ mag), yielding a full spectral energy distribution (SED) at each epoch. The SEDs were then integrated using a trapezoidal integration technique, assuming zero flux at the integration boundaries (the edges of *u* and *K* bands). Finally, the fluxes at each epoch were converted to luminosities assuming our adopted distance to the host galaxy.

For comparison, the OIR pseudo-bolometric light curves of the Type Iax SNe 2005hk (Phillips et al. 2007; Stritzinger et al. 2015, adopting $E(B-V) = 0.11$ mag, $\mu = 33.46 \pm 0.27$ mag), 2012Z (Stritzinger et al. 2015, $E(B-V) = 0.11$ mag, $\mu = 32.59 \pm 0.09$ mag), 2010ae (Stritzinger et al. 2014, $E(B-V) = 0.62$ mag, $\mu = 30.58 \pm 0.58$ mag) and 2008ha (Foley et al. 2009; Valenti et al. 2009; Stritzinger et al. 2014, $E(B-V) = 0.30$ mag, $\mu = 31.64 \pm 0.15$ mag) were computed with the same prescription, using the optical and NIR photometry found in the literature.

For SN 2002cx, only *BVRIr* photometry is available (Li et al. 2003, $E(B-V) = 0.034$ mag, $\mu = 35.09 \pm 0.32$ mag), but given the striking photometric similarities between SNe 2002cx and 2014ck

[7] The abbreviation UVOIR is used with different meanings in the literature. In this paper we use it to mean the flux integrated from 1600 Å (*Swift*/UVOT *uvw2*-band) to 25 μm (*K* band). If the integration starts from 3000 Å (ground-based *U*/*u*-band) we use the label OIR.

Downloaded from https://academic.oup.com/mnras/article/459/1/1018/2609052 by CIS Psicologia Biblioteca F.Metelli - Universita degli Studi di Padova user on 30 September 2020

Table 8. Optical light-curve parameters for SN 2014ck, with associated errors in parentheses.

Filter	Peak MJD	$m_{\rm Peak}$ (mag)	$M_{\rm Peak}$ (mag)	Δm_{15} (mag)	$t_{\rm rise}$ (d)
B	56845.05 (0.50)	16.87 (0.01)	−17.37 (0.15)	1.76 (0.15)	$16.9^{+4.5}_{-2.7}$
g	56846.31 (0.15)	16.65 (0.04)	−17.42 (0.15)	1.59 (0.10)	$18.1^{+4.5}_{-2.7}$
V	56845.60 (0.10)	16.41 (0.01)	−17.29 (0.15)	0.88 (0.05)	$17.4^{+4.5}_{-2.7}$
r	56846.62 (0.20)	16.20 (0.03)	−17.29 (0.15)	0.58 (0.05)	$18.4^{+4.5}_{-2.7}$
i	56849.20 (0.60)	16.08 (0.02)	−17.04 (0.15)	0.39 (0.15)	$21.0^{+4.5}_{-2.7}$

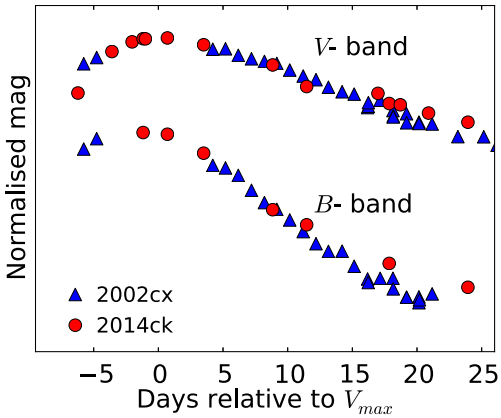

Figure 4. Comparison of normalized (to maximum magnitude) B- and V-band light curves of SNe 2002cx and 2014ck.

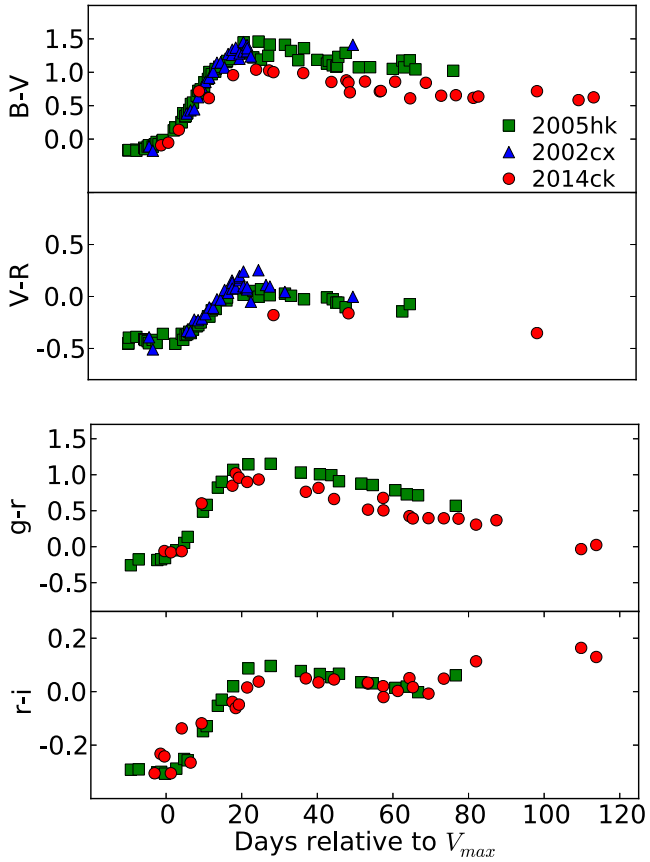

Figure 5. From top to bottom: $B-V$ and $V-R$ (Vega mag), $g-r$ and $r-i$ (AB mag) extinction-corrected colours of SN 2014ck compared with those of SN 2002cx (blue triangles) and SN 2005hk (green squares).

(see Figs 4 and 5), we assume the u and NIR bands give the same contribution to the total flux (at least near maximum light) for both objects. This contribution was estimated from the ratio in flux between the OIR and $BVri$-band bolometric light curves constructed for SN 2014ck, which is around 1.35 at maximum light and decreases to 1.08 ten days after maximum, and applied to SN 2002cx.

Assuming that the light curve is powered by energy deposition from the ^{56}Ni → ^{56}Co → ^{56}Fe radioactive decay chain, the amount of ^{56}Ni synthesized during the explosion can be estimated using Arnett's rule (Arnett 1982). We applied the Stritzinger & Leibundgut (2005) analytic expression for deriving the energy input from the decay of ^{56}Ni evaluated at the time of bolometric maximum (their equation 6). From the observed peak luminosity of SN 2014ck, $L_{\rm max} = 1.91^{+0.30}_{-0.26} \times 10^{42}$ erg s^{-1}, and rise time, $t_{\rm rise} = 16.9^{+4.5}_{-2.7}$ d (cf. Sections 6.1 and 6.2), we obtain $M_{\rm Ni} \simeq 0.09^{+0.04}_{-0.03}\,{\rm M}_{\odot}$. The uncertainty includes the error both in the determination of the rise time and in the adopted distance, which contribute ∼20 per cent and ∼16 per cent, respectively, to the total error budget of the bolometric flux.

In principle, the contribution of UV light to the bolometric luminosity of SNe Ia can be significant, particularly at the earliest epochs when the high temperature yields a large UV flux (Brown et al. 2009; Brown, Roming & Milne 2015), affecting the calculated amount of $M_{\rm Ni}$. In the absence of UV data for SN 2014ck, it is interesting to note that SN 2005hk was already fading in the UV when *Swift* observations began, nearly 10 d before the optical maximum (Phillips et al. 2007; Brown et al. 2009). Similarly, the UV light curves of SN 2012Z reach maximum well before the optical light curves (Stritzinger et al. 2015). For both of them, the bolometric flux is dominated by the optical flux; the flux in the UV drops well below 10 per cent of the total flux before maximum. The same percentage was found for normal SNe Ia (Suntzeff 1996; Contardo, Leibundgut & Vacca 2000; Brown et al. 2009). Thus, considering a maximum additional correction of ∼10 per cent for the contribution of the UV flux at $L_{\rm max}$, the $M_{\rm Ni}$ estimate for SN 2014ck increases to $\simeq 0.10^{+0.04}_{-0.03}\,{\rm M}_{\odot}$, but remains significantly lower than the typical values for normal SNe Ia (∼0.2 to 0.8 $\,{\rm M}_{\odot}$; see Stritzinger et al. 2006a,b; Hayden et al. 2010).

The rise time inferred for SN 2014ck and the extremely low expansion velocity of the ejecta ($v_{\rm ph} \simeq 3.0 \times 10^3$ km s^{-1}, see Section 7), suggest low ejecta mass ($M_{\rm ej}$) and kinetic energy ($E_{\rm k}$) compared to normal SNe Ia and also to SN 2002cx (for which $v_{\rm ph} \simeq 6.0 \times 10^3$ km s^{-1}; see Li et al. 2003). Using Arnett's equations (Arnett 1982) as per Valenti et al. (2008) – a typo in their equation (2) was corrected by Wheeler et al. (2015) – the OIR bolometric light curve is consistent with $M_{\rm ej} \sim 0.2$ to $0.5\,{\rm M}_{\odot}$, placing SN 2014ck close to the cluster made of Type Iax SNe 2002cx, 2008A, 2005hk and 2009ku, just below the fast declining peculiar 1991bg-like

Downloaded from https://academic.oup.com/mnras/article/459/1/1018/2609052 by CIS Psicologia Biblioteca F.Metelli - Universita degli Studi di Padova user on 30 September 2020

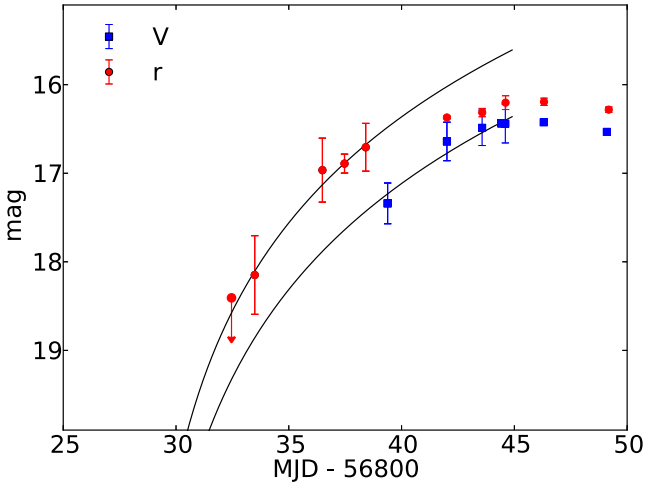

Figure 6. Power-law fit to the five pre-maximum *r*- and *V*-band points using an 'expanding fireball' model (index of the power law $n = 2$). For comparison, a few post-maximum epochs are also shown, although they are not included in the fit.

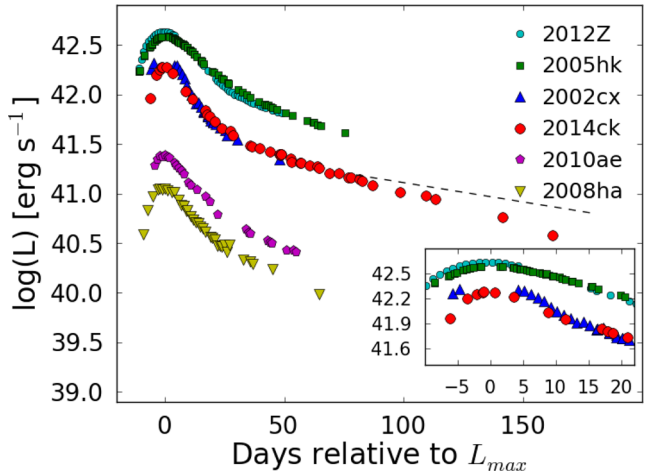

Figure 7. OIR bolometric light curve of SN 2014ck, computed by integrating the fluxes from the *uBVgrizJHK* bands. For comparison the OIR light curves are also shown for the Type Iax SNe 2002cx (Li et al. 2003; Phillips et al. 2007), 2005hk (Phillips et al. 2007; Stritzinger et al. 2015), 2008ha (Foley et al. 2009; Valenti et al. 2009; Stritzinger et al. 2014), 2010ae (Stritzinger et al. 2014) and 2012Z (Stritzinger et al. 2015).

SNe Ia, in the M_{ej} versus M_{Ni} plane plotted in fig. 15 of McCully et al. (2014b).

With regard to the reliability of the M_{ej} estimate, it is well known that the opacities have a strong dependence on the temperature, and therefore that they vary with time (Hoeflich, Khokhlov & Mueller 1992). Hotter, more luminous events should be characterized by higher opacities (Hoeflich et al. 1996; Nugent et al. 1997; Pinto, Eastman & Rogers 2001; Maeda et al. 2003; Baron et al. 2012). We stress that molecules, such as CO, that are predicted to form efficiently in SNe Iax (and, in general, in sub-luminous SNe Ia, see Hoeflich, Khokhlov & Wheeler 1995), do not provide significant opacity in the OIR spectral range. Hence, the above value of M_{ej} should be considered a lower limit, as discussed by Stritzinger et al. (2015) for SN 2012Z.

7 SPECTRAL EVOLUTION

7.1 Optical spectroscopy from −6.0 to +110 d

The spectral evolution of SN 2014ck at optical wavelengths is shown in Figs 8, 9 and 13. There is no sign of helium or hydrogen features. The pre-maximum spectra plotted in Fig. 8 exhibit a blue continuum with a weak, narrow Si II λ6355 absorption line – the hallmark of SN Ia – as well as Fe III λλ4404, 5129 and a relatively strong feature at 4670 Å, tentatively identified as C III λ4647. (There is some indication that the early spectra of SNe 2005hk and 2012Z contain C III; see Chornock et al. 2006; Foley et al. 2013.) At the blue end of the spectra, Ca II H&K and Fe II λ4555 are also identified, while redward of 5000 Å, features associated with S II λλ5454, 5640 and C II λλ6580, 7234 are detected. C II absorption lines have been reported in SN 2008ha (Foley et al. 2010b) and possibly identified in SNe 2002cx (Parrent et al. 2011), 2005hk (Chornock et al. 2006), 2007qd (McClelland et al. 2010), 2012Z (Stritzinger et al. 2015; Yamanaka et al. 2015) and several other SNe Iax (Foley et al. 2013, their fig. 23).

To verify the consistency of line identification and photospheric parameters, we make use of the parametrized synthetic-spectrum code SYNOW (Fisher et al. 1997; Branch et al. 2002, 2003, 2004). In short, SYNOW generates a synthetic spectrum, starting from an adopted blackbody continuum temperature (T_{bb}), photospheric expansion velocity (v_{ph}) and, for each selected ion, a few specific parameters (i.e. the optical depth of the reference line; the excitation temperature; the minimum, maximum and optical-depth e-folding velocities; see Branch et al. 2002, 2004). With SYNOW, synthetic spectra were computed to match the observations at different epochs using ions believed to be present in SN 2014ck, following Branch et al. (2004), Jha et al. (2006), Chornock et al. (2006) and Sahu et al. (2008). In particular we included iron-peak elements, intermediate-mass elements (IMEs) and unburned carbon.

Examples of SYNOW spectra are shown in the insets of Fig. 8 (phase −4 d) and in Fig. 10 (phase +1.7 d). For the pre-maximum spectra, $T_{bb} \approx 7000$ K and $v_{ph} \approx 3500\,km\,s^{-1}$ (see Section 7.1.1) were adopted. The parameters for the fit to the +1.7 d spectrum are $T_{bb} = 5600$ K and $v_{ph} = 3000\,km\,s^{-1}$. We included the set of ions and input parameters used by Branch et al. (2004) for the analysis of the early spectra of SN 2002cx, i.e. Fe II, Fe III, Co II, Cr II, Ca II, Na I, Si II, Si III, S II and Ti II (see their tables 1 and 2). C III and C II ions were added in our SYNOW spectral model to obtain reasonable fits to absorption features at ∼4650 Å and ∼6580 and 7230 Å, respectively. This is shown in the insets in the top panel of Fig. 8, where the synthetic models obtained with and without C III and C II ions are compared to the observed −4 d spectrum. Spectra obtained near maximum light contain Fe III features (see the insets around Fe III λλ4404, 5129 in Fig. 10), while soon after maximum Fe III lines have vanished and strong Fe II lines have developed (as already noted for SN 2002cx by Branch et al. 2004).

We tried also to include Sc II, Ni I and Ni II, instead of Fe II and Co II, which might contribute with features blueward of 4000 Å (especially Sc II). However, lines of Fe II produce most of the observed features, and line blanketing by Co II lines is needed to get a reasonable fit in the blue. Na I, Ca II, Mg II and O I produce just one feature each (see Fig. 10).

Carbon is very likely overabundant in the outer layer of SN 2014ck, since in the very early spectra C II and C III are the strongest lines, along with Fe III. The detection of unburned (C+O) material in the ejecta and, specifically, the spectroscopic signatures and velocity

Downloaded from https://academic.oup.com/mnras/article/459/1/1018/2609052 by CIS Psicologia Biblioteca F.Metelli - Universita degli Studi di Padova user on 30 September 2020

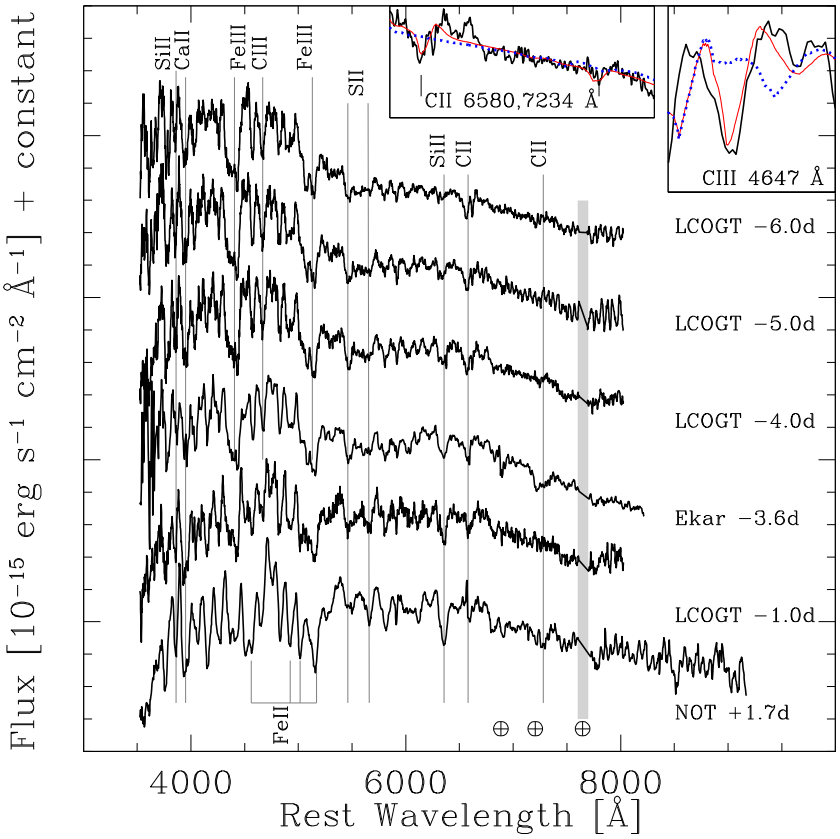

Figure 8. Early spectral evolution and line identification. Phases relative to *V*-band maximum are reported. The insets on the top show regions of the −4 d spectrum centred on C III λ4647 (right) and C II λλ6580, 7234 (left), with the synthetic spectra overplotted, calculated with (solid red curve) and without (dotted blue curve) C II and C III ions (see text for details). Wavelength is in the rest frame, and the positions of major telluric absorption lines are marked with the ⊕ symbol (in particular the vertical grey band marks the strong O_2 *A*-band absorption at 7600 Å).

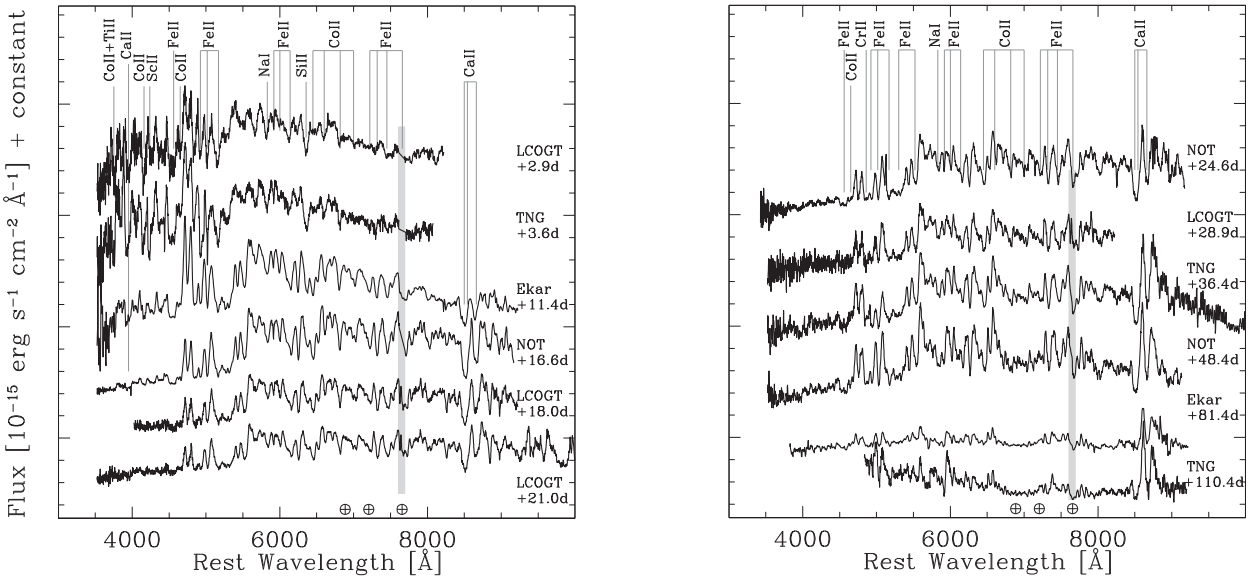

Figure 9. Spectral evolution and line identifications. Phases are reported relative to *V*-band maximum. Left-hand panel: spectra between +2.9 d and +21 d. Right-hand panel: spectra between +24.6 d and +110.4 d. Wavelength is in the rest frame and the positions of major telluric absorption features are marked with the ⊕ symbol (in particular the vertical grey band marks the strong O_2 *A*-band absorption at 7600 Å).

structure of C, is of great importance for constraining our understanding of the explosion mechanisms. In particular, it might be related to the mechanism by which the explosive flame propagates throughout the WD star (Parrent et al. 2011; Folatelli et al. 2012) and/or the type of progenitor system (C/O WD or O/Ne/Mg WD; see Nomoto, Kamiya & Nakasato 2013). Actually, the hallmark of pristine material from C/O WD progenitor star is the presence of carbon, as oxygen is also a product of carbon burning. For SN

Downloaded from https://academic.oup.com/mnras/article/459/1/1018/2609052 by CIS Psicologia Biblioteca F.Metelli - Universita degli Studi di Padova user on 30 September 2020

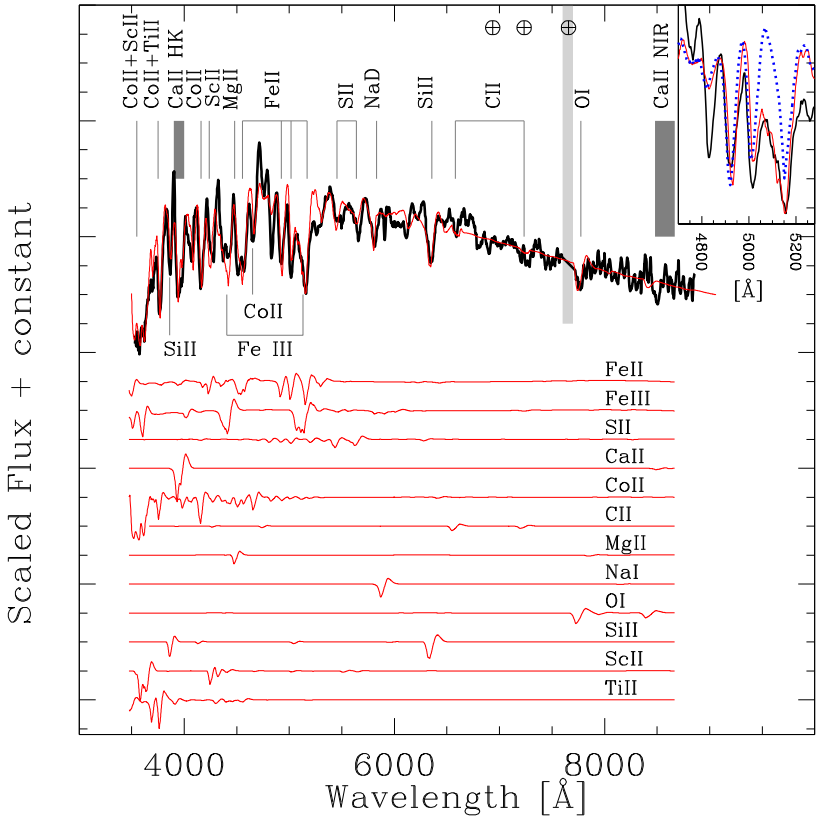

Figure 10. Optical spectrum of SN 2014ck at +1.7 d (black) and our best-fitting SYNOW synthetic spectrum (red). The contribution of each ion is also shown. Major telluric features are indicated with the ⊕ symbol (in particular the vertical grey band marks the strong O_2 *A*-band absorption at 7600 Å). The insets on the right of the plot show the regions around Fe III λ4404 (bottom) and Fe III λ5129 (top) with an synthetic spectrum calculated without Fe III overplotted (dotted blue).

2014ck, the measured pseudo-EW (see Folatelli et al. 2012) of C II λ6580 is ∼10 Å at phase −6 d, which decreases to ∼4 Å two days after *V*-band maximum. For comparison, for normal SNe Ia, Folatelli et al. (2012) find a C II λ6580 pseudo-EW of about 4 Å five days before maximum and ∼1 Å at maximum. This supports the findings from the analysis of SNe 2005cc and 2008ha, presented by Foley et al. (2013), where the C II λ6580 signature is quite strong (see also Parrent et al. 2011): a large fraction of unburned material is present in the ejecta of at least some SNe Iax, and almost every SN Iax with a spectrum before or around maximum light has some indication of carbon absorption.

Taking the Si II λ6355 absorption line as indicator of the photospheric velocity at early epochs (Patat et al. 1996), the ratio between the Doppler velocity of C II λ6580 and Si II λ6355 (see Section 7.1.1, Table 9) at maximum is ∼0.95. It was ∼0.89 for SN 2012Z (Stritzinger et al. 2015, their fig. 9) and around 0.6 for SN 2008ha (Parrent et al. 2011). This ratio is generally slightly above unity among SNe Ia (Parrent et al. 2011; Folatelli et al. 2012), indicating either a layered distribution of carbon-rich material or multiple clumps having similar filling factors. On the other hand, a Doppler velocity of C II significantly below that of the photospheric velocity may indicate ejecta asymmetries, as might be the case for SN 2008ha.

The post-maximum spectra show the emergence of several Fe II (and even Co II) lines becoming dominant over a two-week period. Ni I and Ni II might also contribute blueward of 4000 Å, likely blended with numerous Fe II and Co II lines. The Si II λ6355 feature is clearly visible until 15 d after maximum brightness, as in SN 2002cx (Li et al. 2003; Branch et al. 2004). On the other hand, in the case of SN 2008ha and other faint SN Iax, this feature is only visible near maximum light (Foley et al. 2009, 2010b; Valenti et al. 2009; Stritzinger et al. 2014). Carbon features are clearly detected before maximum. From +24.6 d to +110.4 d the spectra are dominated by Fe II and Co II lines, as well as by the progressive emergence of the Ca II NIR triplet.

In Fig. 11, the spectra of SN 2014ck are compared to those of SNe 2002cx and 2008ha at similar phases. Notably, the pre-maximum spectrum of SN 2014ck resembles SN 2008ha (rather than SN 2002cx), with the exception of the Si II λ6355 absorption line which is clearly stronger in SN 2008ha. 25 d after maximum brightness, the Ca II NIR triplet in SN 2014ck is as strong as in SN 2008ha (Valenti et al. 2009), while this feature is much weaker in SN 2002cx. Around 50 d after maximum, [Ca II] λλ7291, 7324 emission lines begin to emerge. At similar phases, these forbidden lines are stronger in SN 2008ha and extremely weak in SN 2002cx. Overall, the spectra of SN 2014ck show a strong similarity to SN 2008ha and clear differences from SN 2002cx, particularly due to the smaller expansion velocities, but possibly also due to different ejecta composition and opacity.

The very low expansion velocity of SN 2014ck may enhance the visibility of Sc II, tentatively identified in the narrow-line SNe 2007qd (McClelland et al. 2010) and 2008ha (Foley et al. 2009; Valenti et al. 2009).

7.1.1 Expansion velocities of the ejecta

One of the main properties of SNe Iax is the low expansion velocity of the ejecta, which suggests low explosion energies compared to

Downloaded from https://academic.oup.com/mnras/article/459/1/1018/2609052 by CIS Psicologia Biblioteca F.Metelli - Universita degli Studi di Padova user on 30 September 2020

Table 9. Blackbody temperatures (Kelvin) and expansion velocities of the ejecta (km s^{-1}) at the absorption feature minimum for various ions in SN 2014ck. Estimated uncertainties are in parentheses. Phase is from the adopted epoch of the *V*-band maximum, MJD = 56845.6 ± 0.1.

Phase (d)	T_{bb} (K)	Si II λ6355	Ca II H&K	Ca II λ8498	C II λ6580	C II λ7234	S II λλ5454, 5640	O I λ7774	Fe III λ5129	Fe II λ6149	Fe II λ6247	Co II λ15759	Co II λ16064	Co II λ16361
−6.0	8140(100)	3445(50)	4110(200)	3970(200)	3390(50)	3460(100)	3180(100)	3826(50)	3200(100)	5300(200)	4740(200)	–	–	–
−5.0	7340(100)	3339(50)	3800(100)	3760(200)	3030(50)	–	2797(100)	3200(50)	3000(100)	5200(200)	4700(200)	–	–	–
−4.0	6720(100)	2950(50)	3540(100)	–	2935(100)	3130(100)	2395(100)	3020(50)	2820(100)	4690(100)	4620(100)	–	–	–
−3.6	6900(100)	2890(50)	3450(100)	3400(200)	2800(50)	2960(100)	–	2962(50)	–	4590(100)	4500(100)	–	–	–
−3.0	6300(200)	2611(50)	3305(200)	–	2800(50)	2960(100)	–	2866(50)	–	4490(100)	4200(100)	–	–	–
−1.0	5800(200)	–	–	–	–	–	–	–	–	–	–	–	–	–
−1.0	–	–	–	–	–	–	–	–	–	–	–	2700(200)	2360(200)	2450(200)
−0.1	–	2610(100)	3140(200)	3100(200)	–	–	–	2750(50)	–	4180(100)	3800(100)	2656(200)	2262(200)	2339(200)
1.2 7	5630(200)	2560(100)	–	–	–	–	–	–	–	4008(100)	3350(100)	–	–	–
2.9	5360(200)	2430(100)	–	–	–	–	–	2600(50)	–	3800(100)	3160(100)	–	–	–
3.6	5360(200)	–	–	–	–	–	–	–	–	–	–	–	–	–
3.9	–	2250(100)	2800(200)	2700(200)	–	–	–	–	–	3311(100)	3201(100)	2613(200)	2243(200)	2357(200)
5.0	5050(300)	–	–	–	–	–	–	2300(50)	–	2700(100)	2707(100)	–	–	–
11.4	4800(300)	–	–	–	–	–	–	1900(50)	–	2404(100)	2418 (100)	–	–	–
16.6	4500(300)	–	–	–	–	–	–	–	–	2224(100)	2313(100)	–	–	–
18.0	4100(300)	–	–	–	–	–	–	–	–	–	–	–	–	–
19.0	–	–	–	–	–	–	–	–	–	2137(100)	2180(100)	1955(50)	1965(50)	1938(50)
20.0	4110(300)	–	–	–	–	–	–	–	–	2107(100)	2246(100)	–	–	–
21.0	4050(300)	–	–	–	–	–	–	–	–	–	–	–	–	–
23.7	–	–	–	–	–	–	–	–	–	2079(100)	2146(100)	1776(50)	1835(50)	1865(50)
24.6	4070(300)	–	–	–	–	–	–	–	–	2011(100)	2132(100)	–	–	–
28.9	4130(300)	–	–	–	–	–	–	–	–	–	–	–	–	–
30.8	–	–	–	–	–	–	–	–	–	1740(100)	1769(100)	1634(50)	1742(50)	1683(50)
36.4	4110(300)	–	–	–	–	–	–	–	–	1919(100)	1950(100)	–	–	–
39.0	–	–	–	–	–	–	–	–	–	–	–	–	–	–
46.8	–	–	–	–	–	–	–	–	–	1613(100)	1680(100)	–	–	–
48.4	4120(300)	–	–	–	–	–	–	–	–	1580(100)	1511(100)	–	–	–

Downloaded from https://academic.oup.com/mnras/article/459/1/1018/2609052 by CIS Psicologia Biblioteca F.Metelli - Universita degli Studi di Padova user on 30 September 2020

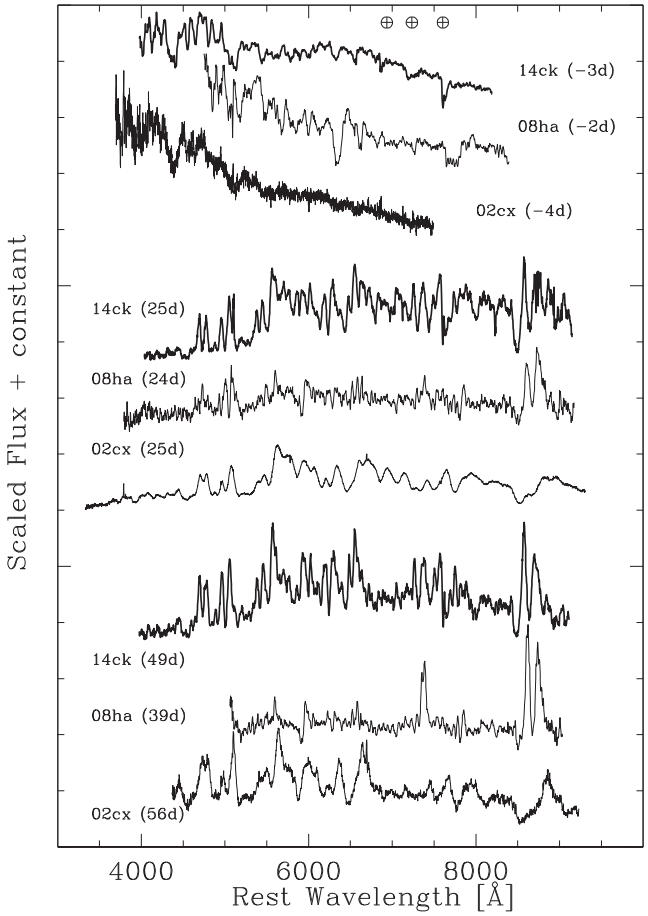

Figure 11. Comparison of the rest-frame spectra of SN 2014ck at phases −3.5 d, +25 d and +48 d with those of SNe 2002cx (Li et al. 2003; Phillips et al. 2007) and 2008ha (Foley et al. 2009; Valenti et al. 2009) at similar phases.

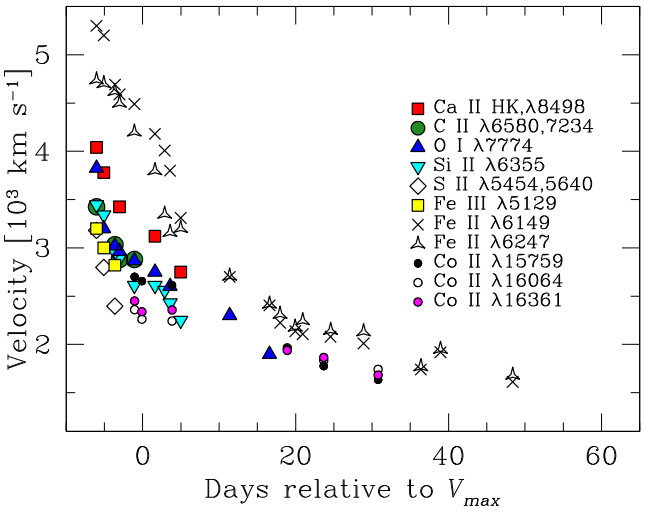

Figure 12. Velocity evolution of the absorption minima of a selection of spectral lines with minimal line blending in the spectra of SN 2014ck. The typical formal error of the velocities is ∼200 km s^{-1}. The blending of lines can produce a systematic shift of features and increase the uncertainty at least to ∼1000 km s^{-1}.

normal SNe Ia (see Section 6.3). The ejecta velocity of SN 2014ck was estimated from the location of the absorption minima of spectral lines with little line blending, based on line identifications from SYNOW.

The results are listed in Table 9 and plotted in Fig. 12. Early spectra can be used to probe the velocity distribution of various elements, i.e. unburned (C+O) material, IMEs and completely burned elements close to nuclear statistical equilibrium, namely iron, cobalt and nickel. In principle, the velocity evolution can provide solid constraints on the explosion physics, as a layered structure might be revealed (a signature of detonations, Stritzinger et al. 2014, 2015) unless extensive mixing has destroyed the original stratification (a signature of deflagrations; Phillips et al. 2007). However, for SNe Iax there is severe blending of lines over the full optical and NIR spectral range that prevent secure line identifications and plague our velocity estimates (Szalai et al. 2015).

Before maximum light, expansion velocities are measured from the minima of Ca II H&K and λ8498; C II λλ6580, 7234; S II λλ5454, 5640; and Si II λ6355 absorption features and are found to lie between 2800 and 4100 km s^{-1}. Mg II λ4481 soon becomes blended with Fe III and is not easily distinguished. On the contrary, the O I line at λ7774 is clearly detected redward of the telluric *A*-band at 7590–7650 Å and the calculated velocities are similar to the ones inferred for Si II. At these early phases, iron features Fe II λλ6149, 6247 and 4555 exhibit consistent line velocities that are ∼1000 km s^{-1} higher than those of IMEs and Fe III λ5129. However, we note that complex blending with emerging Co II and Ti II features could change the position of Fe III λ5129 (and also Fe III λ4404) absorption minima.

Indeed, around maximum light, the blending with emerging Fe II, Ti II and Co II lines might broaden the observed profile and shift the middles of several lines. In particular, even during pre-maximum phases, the feature around 6300 Å, mainly attributed to Si II λ6355, could be a blend with Fe II λ6456 (or a more complex blending either with Fe II plus Co II or S II; see Szalai et al. 2015, their figs 11 and 12). After maximum, the 'iron curtain' prevents the secure identification of unburned (C+O) material or IMEs, forming at similar or higher velocities (Branch et al. 2004), and the velocity measurements might be ill constrained. Close to maximum, the absorption-minimum velocities of the Co II NIR lines at 1.5759, 1.6064 and 1.6361 μm are in good agreement either with Si II λ6355 or S II λλ5454, 5640, and are ∼2000 km s^{-1} lower than for Fe II λλ6149, 6247.

About 20 d after maximum, the velocities of the Co II NIR features are systematically ∼300 km s^{-1} lower than those inferred from optical Fe II lines at the same phase. A similar trend was noted by Stritzinger et al. (2014) for SN 2010ae. Hereafter the line velocities evolve rather slowly.

Overall, the velocity structure of SN 2014ck indicates outer layers rich in iron-group ions, while C+O elements, Si II and Ca II, identified at lower velocities, seem to be well mixed. In principle, they should be present even at higher velocities (i.e. in the outer layers) if earlier spectra were available for an in-depth analysis. Consequently, we cannot exclude either a mixed or a layered structure for SN 2014ck and, in turn, it is not easy to discriminate between the different explosion mechanisms (see Section 8).

In Table 9, we also list our estimates of the photospheric temperature of SN 2014ck as derived from a blackbody fit to the spectral continuum (the spectra were corrected for the redshift and extinction). At phases beyond +50 d, emerging emission lines and line blanketing drive a flux deficit at the shorter wavelengths, and the fit becomes difficult. The errors are estimated from the dispersion

Downloaded from https://academic.oup.com/mnras/article/459/1/1018/2609052 by CIS Psicologia Biblioteca F.Metelli - Universita degli Studi di Padova user on 30 September 2020

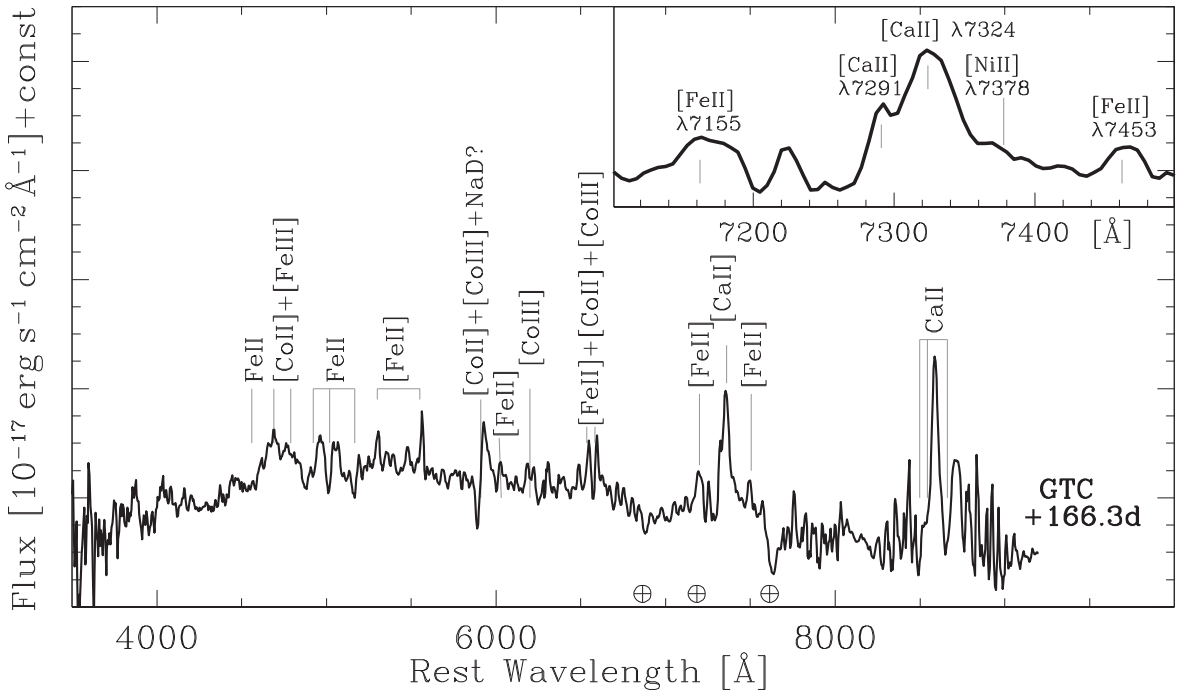

Figure 13. Late-phase spectrum of SN 2014ck with line identification based on Li et al. (2003), Jha et al. (2006) and Sahu et al. (2008). The inset shows the region around ∼7300 Å, where forbidden [Ca II] λλ7291, 7324 and [Fe II] λλ7155, 7453features are clearly identified. [Ni II] λ7378 might be present in the red wing of [Ca II] λ7324.

of measurements obtained with different choices for the spectral fitting regions. The early photospheric temperature of SN 2014ck is above 8000 K, but it decreases quickly to ∼5600 K at maximum light and flattens to about 4000 K afterwards.

7.2 The late-time spectrum at +166.3 d

A late-phase spectrum of SN 2014ck was obtained at +166.3 d and is plotted in Fig. 13. As already remarked for other SNe Iax (Foley et al. 2013), the late-phase spectrum does not appear to be truly nebular despite no clear indication of a continuum or absorption lines. At these late epochs, SN 2014ck shows narrow permitted Fe II lines superimposed on a pseudo-continuum and several forbidden lines associated with of Fe, Co and Ca. The dominant feature is the Ca II NIR triplet, but also comparable in strength is the forbidden [Ca II] λλ7292, 7324 doublet (see Fig. 13). Both permitted and forbidden calcium lines are significantly more prominent in SN 2014ck than in SN 2002cx, and are comparable to those of the fainter SNe 2008ha and 2010ae (Foley et al. 2009; Valenti et al. 2009; Stritzinger et al. 2014). The [Fe II] λ7155 line is the strongest iron feature in the late-time spectrum. A relatively broad hump at 4700 Å is identified as [Fe III] and [Co II].

A number of features blueward of 5800 Å are likely a blend of permitted Fe II lines. The same lines are present at earlier epochs but at higher velocities. This identification was suggested by Jha et al. (2006) for SN 2002cx. As a test, we attempted to fit the late-time spectrum with a SYNOW model, including Fe II, Ca II, Na I and O I ions (see Jha et al. 2006, their table 2 and their figs 3 and 4). Although the observed spectrum is not fully reproduced by the photospheric model, the synthetic spectrum provides a good match to many of the absorption features blueward of 5800 Å, and possibly the P-Cygni profiles of Na I D at λλ5890, 5896. An alternative identification of this feature could be [Co III] λ5888 (Dessart et al. 2014), also suggested for SN 2012Z by Stritzinger et al. (2015). This last interpretation is supported by the unambiguous presence of other [Co III] lines in the 6000 Å region.

We conclude that the late-time spectrum of SN 2014ck is a combination of P-Cygni profiles of recombination lines and emission lines of forbidden Fe, Ca and Co features, but no [O I] λλ6300, 6364 emission. This feature is typically not present in late spectra of SNe Ia (Blondin et al. 2012). In order to get [O I] emission, we need a significant amount of O in a region where γ-rays are being absorbed, and the O-emitting region cannot be too contaminated by Ca. In fact, the [Ca II] λλ7291, 7324 feature can limit the strength of [O I] λλ6300, 6364 emission from a region in which both these ions co-exist (Fransson & Chevalier 1989; Dessart & Hillier 2015). The emission of [O I] λλ6300, 6364 is absent from relatively late spectra of SNe 2014ck and 2008ha (Foley et al. 2009), while in both cases O I λ7774 absorption is identified in photospheric phase spectra.

The FWHM values were estimated as 1900, 1200and 1600 km s^{-1} for the [Ca II], [Fe II] and Ca II NIR lines, respectively. The nebular lines have slightly diverse velocity shifts: about +170 km s^{-1} for [Fe II] λλ7155, 7453, −270 km s^{-1} for [Ca II] λλ7291, 7324 and −180 km s^{-1} for [Ni II] λ7376 (the latter is difficult to measure as it is in the wing of [Ca II]). As already noted by Foley et al. (2013) for SNe 2002cx, 2005hk, 2008A and 2008ge, the [Fe II] and [Ca II] features have shifts in opposite directions, highlighting a quite complex velocity structure of SNe Iax.

7.3 NIR spectral sequence

The NIR spectral evolution of SN 2014ck is presented in Fig. 14. Before maximum light, large parts of the spectra resemble the infrared tail of a hot blackbody continuum, with the exception of few spectral features around 1 μm and humps between 1.5 and 1.8 μm.

Downloaded from https://academic.oup.com/mnras/article/459/1/1018/2609052 by CIS Psicologia Biblioteca F.Metelli - Universita degli Studi di Padova user on 30 September 2020

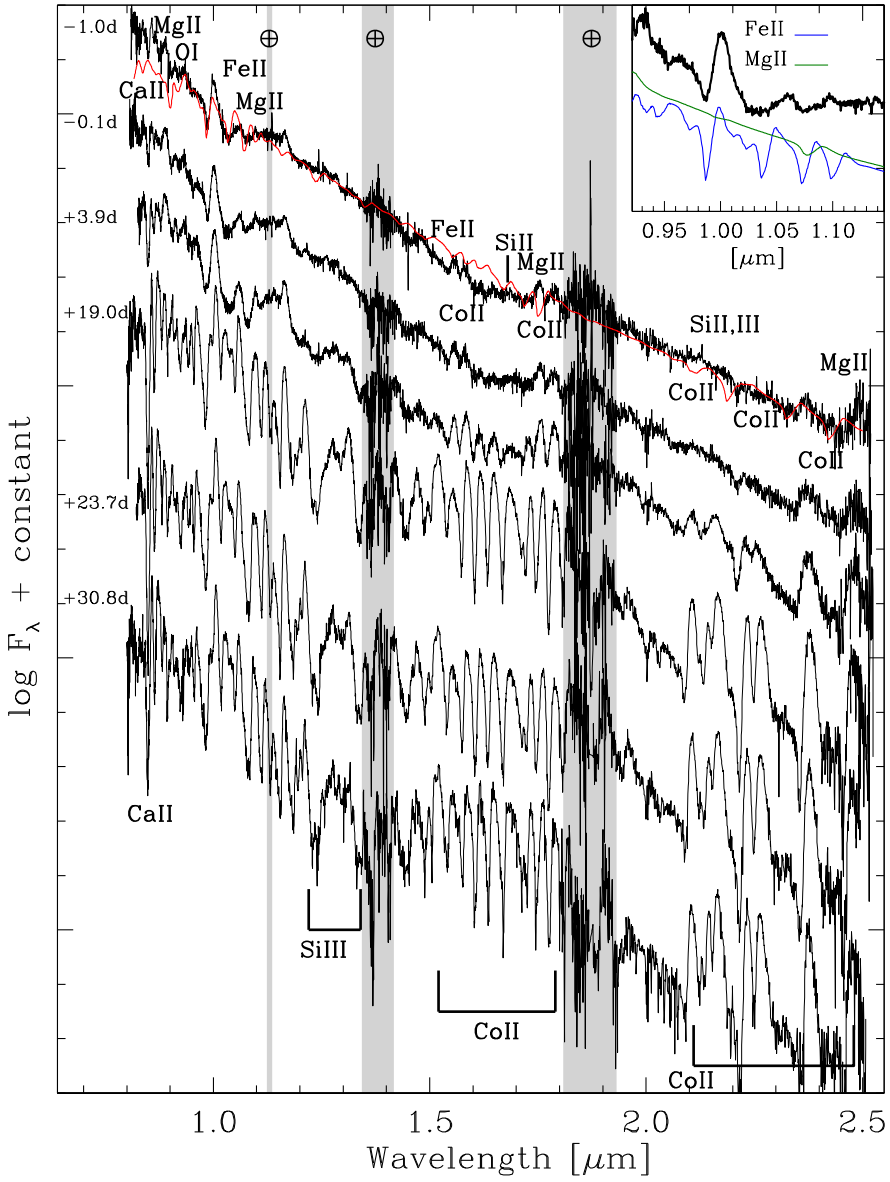

Figure 14. NIR spectra of SN 2014ck obtained with the Gemini North Telescope (+ GNIRS). The phase relative to *V*-band maximum is labelled for each spectrum. Prevalent features attributed to Fe II, Mg II, Ca II, Co II and Si III are indicated with labels. Telluric regions are indicated with the ⊕ symbol and vertical grey bands. The −1 d spectrum is compared to our best-fit SYNOW synthetic spectrum (red). The inset on the top shows the +0.4 d spectrum (black) in the range 0.95 to 1.15 μm, showing the main features due to Fe II (blue) and Mg II (green).

From −0.1 d to +3.9 d, the most prominent features are attributed to Fe II, in particular the stronger line with a P-Cygni profile at ∼1 μm is Fe II 0.9998 μm. Mg II 0.9227 and 1.0927 μm (and possibly weaker lines around 2.4 μm due to Mg II transitions, i.e. 2.4041, 2.4044, 2.4125 μm; see Höflich et al. 2002) produce shallow notches partially blended with Fe. Moreover, also around 1 μm, there might be traces of C I lines at 0.9093, 0.9406, 1.0693 and 1.1754 μm, which have been tentatively identified both in the sub-luminous Type Ia SN 1999by (Höflich et al. 2002) and in the Type Iax SN 2012Z (Stritzinger et al. 2015), in addition to normal SNe Ia (Hsiao et al. 2013, 2015). However, no confident carbon detections can be made in SN 2014ck NIR spectra. O I 0.9264 μm should be blended with Mg II 0.9227 μm. Actually, in our optical spectra the O I λ7773 – which is expected to be 3–20 times stronger than the 0.9264 μm line – is already weak, so the O I 0.9264 μm is not expected to be a strong feature. The 0.8446 μm O I line may contribute to the absorption, dominated in later phases by the Ca II NIR triplet. Signatures of Si II might be present blueward of 1 μm (0.9413 μm) and the 1.6930 μm Si II line may be part of the hump at these wavelengths, together with Mg II (1.6787 μm) and emerging Co II lines. A SYNOW fit (adopting $T_{bb} = 5800$ K and $v_{ph} = 2500$ km s^{-1}, see Section 7.1.1) of the −1 d spectrum was used to assist for the above line identification, including an extended set of ions (C I, C II, O I, Mg I, Mg II, Si II, Si III, Ca II, Fe II, Fe III and Co II, see Fig. 14). The inset of Fig. 14 shows the most prominent feature in the earliest spectrum, attributed to Fe II 0.9998 μm.

Three weeks later, the NIR spectrum radically changes, being strongly dominated by Co II lines, as previously documented in all other SNe Iax with similar data (Kromer et al. 2013; Stritzinger et al. 2014, 2015). Co II clearly contributes with numerous lines between 1.6 and 1.8 μm soon after maximum light, as it is already present in the spectrum taken at +3.9 d. Spectra obtained at +19 d

Downloaded from https://academic.oup.com/mnras/article/459/1/1018/2609052 by CIS Psicologia Biblioteca F.Metelli - Universita degli Studi di Padova user on 30 September 2020

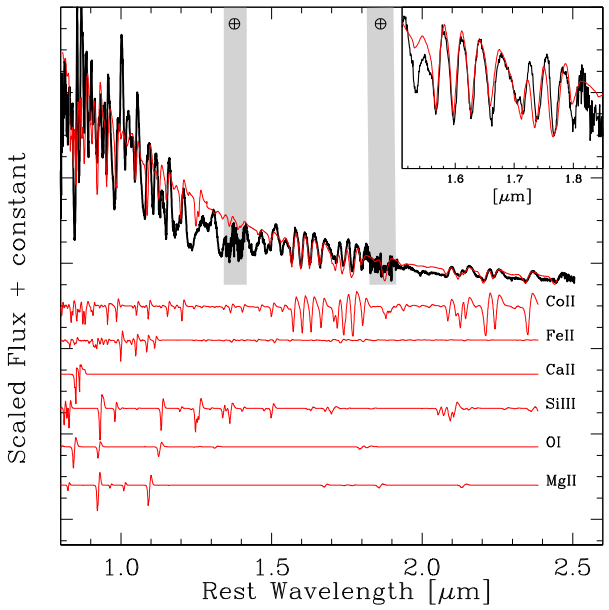

Figure 15. NIR spectrum of SN 2014ck at +19 d (black) and our best-fit SYNOW synthetic spectrum (red). The contribution of prevalent ions is also shown. Telluric regions are indicated with the ⊕ symbol and vertical grey bands. Inset: close-up of the *H*-band spectral region, showing the ubiquitous signature of Co II.

or later show distinct absorption at the location of several Co II lines, most prominently at 1.5759, 1.6064, 1.6361, 1.7772, 1.7462, 2.2205, 2.4596 and 2.3613 μm. The increasing strength of Co II with time is attributed both to a lower opacity and a higher abundance of ^{56}Co in the external ejecta compared with SNe Ia (Hsiao et al. 2013). The SYNOW fit to the +19 d spectrum of SN 2014ck is plotted in Fig. 15. We adopted $T_{bb} = 4000$ K and $v_{ph} = 1900\,km\,s^{-1}$ (see Section 7.1.1) and included a smaller sub-set of the above IMEs and Fe-group ions (Co II, Fe II, Ca II, Si III, O I and Mg II). While it is confirmed that Co II largely dominates the spectrum redward of 1.5 μm (*H* and *K* bands), Fe II prevails blueward of that wavelength, as in the spectra of SNe Ia during the transition from the photospheric to the nebular phase (Friesen et al. 2014). The Ca II NIR triplet is also a prevalent feature starting from the spectrum at +19 d, and Si III might help to improve the fit of the features between 1.1 and 1.4 μm (as in SN 2012Z; see Stritzinger et al. 2015).

The NIR spectral evolution of SN 2014ck is reminiscent of what is observed in SN 2010ae (see Stritzinger et al. 2014, their fig. 4) and, overall, in normal SNe Ia (Marion et al. 2009; Hsiao et al. 2013, 2015). For both SNe Ia and SNe Iax, the characteristic *H*- and *K*-band iron-peak complex rapidly emerges soon after *B*-band maximum and becomes the dominant feature in the NIR.

7.4 A summary of the overall spectral characteristics

Similarly to SN 2008ha (Foley et al. 2010b), the pre-maximum spectra of SN 2014ck show the signatures of Si II λλ6347, 6371, S II λλ5454, 5640 (together with Ca, O, Na and Fe) and no sign of hydrogen or helium. As in SN 2008ha, unburned (C+O) material, specifically C II λλ6580, 7234 is also detected, as is C III λ4647. Such analogies in the early phases might suggest they share analogous physical conditions and composition. However, unlike SN 2008ha, the late spectrum of SN 2014ck is dominated by iron-peak elements, with the presence of both permitted Fe II and forbidden [Fe II], [Fe III] and [Co II] emission lines. It also displays relatively strong features of both the Ca II NIR triplet and [Ca II] λλ7291, 7324, which have a comparable strength in SN 2008ha but are weak or absent in SN 2002cx. In the NIR spectral region, SN 2014ck shows features typical of SNe Iax, with the ubiquitous presence of Co II. Fe II lines are present in SN 2014ck at higher expansion velocities than IMEs and unburned C+O elements. Before maximum, Ca II lines velocities are bracketed by measures of Fe II, Fe III and S II.

8 CONCLUDING REMARKS

Mirroring the behaviour already observed for SN 2009ku by Narayan et al. (2011), the high luminosity and low ejecta velocity for SN 2014ck is contrary to the trend generally seen in the heterogeneous group of peculiar SNe Iax. In fact, from a photometric point of view SN 2014ck resembles SN 2002cx, the prototype of the class, showing similar peak luminosities ($M_B = -17.37 \pm 0.15$ mag for SN 2014ck versus $M_B = -17.53 \pm 0.26$ mag for SN 2002cx) and decline rates ($\Delta m_{15}(B) = 1.76 \pm 0.15$ mag versus $\Delta m_{15}(B) = 1.7 \pm 0.1$ mag) in all bands. Given the almost identical bolometric luminosities at maximum, the synthesized mass of ^{56}Ni is nearly the same for both objects, $\sim 0.1\,M_\odot$.

Yet despite the relatively high peak luminosity and slow light-curve decline, the spectra of SN 2014ck are more similar to those of the three-magnitudes-fainter SNe 2008ha (Foley et al. 2009; Valenti et al. 2009), 2007qd (McClelland et al. 2010) and 2010ae (Stritzinger et al. 2014). All these objects exhibit narrow spectral lines indicating low expansion velocities of the ejecta (v_{ph} from 2500 to 3000 km s^{-1} at maximum from the absorption minima of Si II). McClelland et al. (2010) and Foley et al. (2013) suggested the existence of a relation between peak luminosity, ejecta velocity and light-curve shape, with higher velocity SNe Iax being more luminous and more slowly declining. On this basis, they argued that the full class of SNe Iax might originate from a single explosion mechanism.

Both SNe 2009ku and 2014ck, with their low velocity and relatively high luminosity, are outliers in these relations, and the results of this work confirm and reinforce the results of Narayan et al. (2011). This is illustrated in Fig. 16, which shows the positions of a sample of SN Iax in a three-variable phase space composed of $\Delta m_{15}(V)$, M_V and v_{ph} measured 10 d after maximum (see Narayan et al. 2011, their fig. 3). In fact, this sample of SNe Iax shows: (i) there is not a monotonic correlation between v_{ph} and $\Delta m_{15}(V)$, as at low velocities the spread in the decline rate is wide (top-left panel); (ii) there is evidence of a linear correlation between $\Delta m_{15}(V)$ and M_V (bottom-left); and (iii) SN 2014ck (and also SN 2009ku) are at odd with the suggestion of McClelland et al. (2010) that higher velocity SNe Iax also have higher peak luminosities (bottom-right panel). We note that these are still small-number statistics, and therefore these findings need further confirmation. However, at present we cannot conclude SNe Iax are a one-dimensional sequence from fainter to brighter events.

Comprehensive explosion models are required to describe both the diversity and homogeneity among SNe Iax. On the whole, the observations seem to indicate that they may originate from a homogeneous population (Foley et al. 2013). However, specifically, there appears to be a diverse range of rise times, peak luminosities, expansion velocities, etc. and, as underlined above, there is not a clear correlation among these physical parameters. Thus, there may be multiple progenitor paths and explosion mechanisms to create an SN Iax. To date, the progenitors of SNe Iax are still a subject of debate (Foley et al. 2009, 2010b; Valenti et al. 2009; Moriya et al. 2010; Liu et al. 2015b). The search and detection of progenitor

Downloaded from https://academic.oup.com/mnras/article/459/1/1018/2609052 by CIS Psicologia Biblioteca F.Metelli - Universita degli Studi di Padova user on 30 September 2020

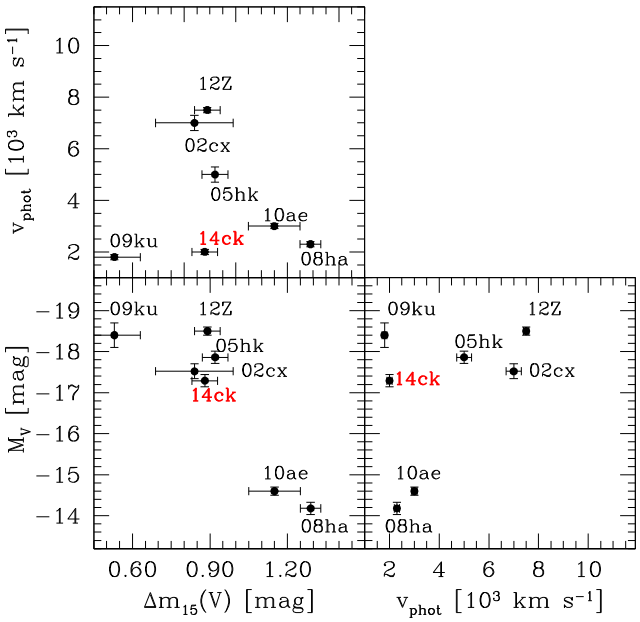

Figure 16. Scatter plots of $\Delta m_{15}(V)$, M_V and photospheric velocities v_{ph} derived around +10 d for several well studied SNe Iax (see Narayan et al. 2011, their fig. 3).

stars or systems in pre-explosion images is, in principle, a promising technique to test different progenitor models (McCully et al. 2014a; Liu et al. 2015a,b). For SN 2014ck, archival *HST* images were obtained and no progenitor was detected at the SN position. The available images are not very deep and provide a 3σ limit of $m_{F625W} > -6.5$ mag. This limit allows us to rule out only the most-luminous Wolf–Rayet stars as a potential progenitor.

Overall, the optical and NIR observational features summarized above favour a thermonuclear explosion of a C/O WD for SN 2014ck. A failed deflagration model (Jordan et al. 2012; Kromer et al. 2013) might explain most of its observed properties, from the low peak luminosity and energetics (see Section 6.3) to the spectral characteristics (see Section 7). In particular, the moderate M_{Ni} production derived for this event and the low expansion velocities are well matched in this scenario. The failed deflagration is too weak to unbind the WD, leaving behind a gravitationally bound, compact remnant around $\sim 1\,M_{\odot}$. The low ejecta mass of SN 2014ck is partially consistent with that prediction. However, the rise time predicted by these models (see table 4 in Fink et al. 2014) is too fast compared to the rise time derived for SN 2014ck ($t_{rise} = 16.9^{+4.5}_{-2.7}$ d, see Section 6.2). Above all, the modelled burning of a C/O WD via a turbulent deflagration flame produces a homogeneous mixing of elements in the ejecta, with unburned material, partially burned material and fully burned (to the iron peak) material throughout the ejecta. Significant mixing in the ejecta was suggested for SN 2005hk by Phillips et al. (2007). The failed deflagration model was also considered the most probable scenario for SN 2012Z by Yamanaka et al. (2015). On the contrary, for the same event, Stritzinger et al. (2015) pointed out evidence of a layered structure for calcium, silicon and magnesium, which is instead the signature of a detonation. Thus, they suggested that these elements are produced in a detonation phase after the mixing has already occurred and the majority of the iron peak elements have been produced in a previous deflagration phase, i.e. a pulsational delayed detonation (PDD; Hoeflich et al. 1995, 1996).

Looking at the velocity distribution of elements in SN 2014ck (Fig. 12), the presence of Fe II features up to high velocities, as reported by Stritzinger et al. (2015) for SN 2012Z (and also for few normal SNe Ia), seems to suggest a layered structure in the ejecta, arguing in favour of a detonation phase, which might have followed a deflagration. On the other hand, C+O elements and Si II are moderately mixed, and one could argue that they would be identified at higher velocities if earlier spectra were available. Moreover, explaining iron-group material in the outer layers is still a challenge for explosion models, even if some results have been obtained within a delayed detonation scenario (see for example Hachinger et al. 2013, and references therein). So far, several questions are still open, among them the mechanism of transition from deflagration to detonation. To be thorough, it is difficult to explain within PDD models the extremely low photospheric velocity at maximum of SN 2014ck. We also underline, once again, that the severe blending across the spectra of SNe Iax, might prevent secure line identifications, as was detailed by Szalai et al. (2015). Consequently, the derived expansion velocities of the elements is ill constrained, as well as the distinction between a layered or a mixed structure of the ejecta.

The analysis of our extended data set of SN 2014ck cannot exclude either the failed deflagration or the PDD models for this event. In addition, the comparison with other SNe Iax highlights that the diversity within this class of transients cannot be reduced to a one-parameter description. This may also imply that distinct progenitors and/or explosion mechanisms are involved, despite the overall similarity of the main observables.

ACKNOWLEDGEMENTS

This paper is based on observations made with: the LCOGT 2.0 m (Haleakala, Hawaii, USA) and 1.0 m (McDonald Observatory, Texas, USA) telescopes; the 2.56 m Nordic Optical Telescope (La Palma, Spain); the INAF Osservatorio Astronomico di Padova Copernico 1.82 m Telescope (Mt. Ekar, Asiago, Italy); the 3.58 m Telescopio Nazionale Galileo (La Palma, Spain); the 8.1 m Gemini-N Telescope (Hilo, Hawaii, USA); and the 10.4 m Gran Telescopio Canarias (La Palma, Spain). We acknowledge the staff at INAF OAPd in Asiago and at LCOGT for their support.

Based on observations obtained at the Gemini Observatory under Program ID GN-2014A-Q-8 and GN-2014B-Q-41. Gemini is operated by the Association of Universities for Research in Astronomy, Inc., under a cooperative agreement with the NSF on behalf of the Gemini partnership: the National Science Foundation (USA), the National Research Council (Canada), CONICYT (Chile), the Australian Research Council (Australia), Ministério da Ciência, Tecnologia e Inovação (Brazil) and Ministerio de Ciencia, Tecnología e Innovación Productiva (Argentina). Also based on observations made with the NASA/ESA *Hubble Space Telescope*, obtained from the data archive at the Space Telescope Science Institute. STScI is operated by the Association of Universities for Research in Astronomy, Inc. under NASA contract NAS 5-26555.

We thank WeiKang Zheng and Alex Filippenko for sending us pre-discovery and discovery Lick/KAIT images of UGC 12182 from which non-detection upper limits of SN 2014ck were determined and the rise time estimated. We also thank the anonymous referee for the thorough review of the paper.

AP, SB, NER, LTar, GT and MT are partially supported by the PRIN-INAF 2014 with the project 'Transient Universe: unveiling new types of stellar explosions with PESSTO'. NER acknowledge the support from the European Union Seventh Framework

Downloaded from https://academic.oup.com/mnras/article/459/1/1018/2609052 by CIS Psicologia Biblioteca F.Metelli - Universita degli Studi di Padova user on 30 September 2020

Programme (FP7/2007-2013) under grant agreement no. 267251 'Astronomy Fellowships in Italy' (AstroFIt). AMG acknowledges financial support by the Spanish *Ministerio de Economía y Competitividad* (MINECO), grant ESP2013-41268-R. MS and EYH acknowledge support provided by the Danish Agency for Science and Technology and Innovation through a Sapere Aude Level 2 grant.

This research has made use of: the NED which is operated by the Jet Propulsion Laboratory, California Institute of Technology, under contract with the National Aeronautics and Space Administration; IRAF packages, distributed by the National Optical Astronomy Observatory, operated by the Associated Universities for Research in Astronomy, Inc. under cooperative agreement with the National Science Foundation; the SDSS-III DR12 (APOGEE-1, BOSS, MARVELS, SEGUE-2) managed by the Astrophysical Research Consortium for the Participating Institutions of the SDSS Collaboration, see the web site www.sdss.org.

REFERENCES

Alam S. et al., 2015, ApJS, 219, 12
Arnett W. D., 1982, ApJ, 253, 785
Baron E., Höflich P., Krisciunas K., Dominguez I., Khokhlov A. M., Phillips M. M., Suntzeff N., Wang L., 2012, ApJ, 753, 105
Blanton M. R., Roweis S., 2007, AJ, 133, 734
Blondin S., Masters K., Modjaz M., Kirshner R., Challis P., Matheson T., Berlind P., 2006, Cen. Bur. Electron. Telegrams, 636, 1
Blondin S. et al., 2012, AJ, 143, 126
Branch D., 1998, ARA&A, 36, 17
Branch D., Fisher A., Nugent P., 1993, AJ, 106, 2383
Branch D. et al., 2002, ApJ, 566, 1005
Branch D. et al., 2003, AJ, 126, 1489
Branch D., Baron E., Thomas R. C., Kasen D., Li W., Filippenko A. V., 2004, PASP, 116, 903
Brown P. J. et al., 2009, AJ, 137, 4517
Brown T. M. et al., 2013, PASP, 125, 1031
Brown P. J., Roming P. W. A., Milne P. A., 2015, J. High Energy Astrophys., 7, 111
Cappellaro E., 2014, SNOoPy: a Package for SN photometry, version 0.5. Available at: http://sngroup.oapd.inaf.it/snoopy.html
Cardelli J. A., Clayton G. C., Mathis J. S., 1989, ApJ, 345, 245
Chonis T. S., Gaskell C. M., 2008, AJ, 135, 264
Chornock R., Filippenko A. V., Branch D., Foley R. J., Jha S., Li W., 2006, PASP, 118, 722
Contardo G., Leibundgut B., Vacca W. D., 2000, A&A, 359, 876
Crowther P. A., 2007, ARA&A, 45, 177
Dessart L., Hillier D. J., 2015, MNRAS, 447, 1370
Dessart L., Hillier D. J., Blondin S., Khokhlov A., 2014, MNRAS, 439, 3114
Dolphin A. E., 2000, PASP, 112, 1383
Falco E. E. et al., 1999, PASP, 111, 438
Feldman H. et al., 2003, ApJ, 596, L131
Filippenko A. V. et al., 1992a, AJ, 104, 1543
Filippenko A. V. et al., 1992b, ApJ, 384, L15
Filippenko A. V., Li W. D., Treffers R. R., Modjaz M., 2001, in Paczynski B., Chen W.-P., Lemme C., eds, ASP Conf. Ser. Vol. 246, IAU Colloq. 183: Small Telescope Astronomy on Global Scales. Astron. Soc. Pac., San Francisco, p. 121
Fink M. et al., 2014, MNRAS, 438, 1762
Firth R. E. et al., 2015, MNRAS, 446, 3895
Fisher A., Branch D., Nugent P., Baron E., 1997, ApJ, 481, L89
Folatelli G. et al., 2012, ApJ, 745, 74
Foley R. J. et al., 2009, AJ, 138, 376
Foley R. J. et al., 2010a, AJ, 140, 1321
Foley R. J., Brown P. J., Rest A., Challis P. J., Kirshner R. P., Wood-Vasey W. M., 2010b, ApJ, 708, L61
Foley R. J. et al., 2013, ApJ, 767, 57
Foley R. J., Van Dyk S. D., Jha S. W., Clubb K. I., Filippenko A. V., Mauerhan J. C., Miller A. A., Smith N., 2015, ApJ, 798, L37
Foreman-Mackey D., Hogg D. W., Lang D., Goodman J., 2013, PASP, 125, 306
Fransson C., Chevalier R. A., 1989, ApJ, 343, 323
Friesen B., Baron E., Wisniewski J. P., Parrent J. T., Thomas R. C., Miller T. R., Marion G. H., 2014, ApJ, 792, 120
Ganeshalingam M., Li W., Filippenko A. V., 2011, MNRAS, 416, 2607
Gonzaga S. et al., 2012, HST Data Handbook. STScI, Baltimore, MD
Hachinger S. et al., 2013, MNRAS, 429, 2228
Hamuy M., Phillips M. M., Maza J., Suntzeff N. B., Schommer R. A., Aviles R., 1995, AJ, 109, 1
Hamuy M., Phillips M. M., Suntzeff N. B., Schommer R. A., Maza J., Aviles R., 1996a, AJ, 112, 2391
Hamuy M., Phillips M. M., Suntzeff N. B., Schommer R. A., Maza J., Smith R. C., Lira P., Aviles R., 1996b, AJ, 112, 2438
Hayakawa G. K., Zheng W., Filippenko A. V., 2014, Cen. Bur. Electron. Telegrams, 3949, 1
Hayden B. T. et al., 2010, ApJ, 712, 350
Hoeflich P., Khokhlov A., Mueller E., 1992, A&A, 259, 549
Hoeflich P., Khokhlov A. M., Wheeler J. C., 1995, ApJ, 444, 831
Hoeflich P., Khokhlov A., Wheeler J. C., Phillips M. M., Suntzeff N. B., Hamuy M., 1996, ApJ, 472, L81
Höflich P., Gerardy C. L., Fesen R. A., Sakai S., 2002, ApJ, 568, 791
Hsiao E. Y. et al., 2013, ApJ, 766, 72
Hsiao E. Y. et al., 2015, A&A, 578, A9
Jha S., Branch D., Chornock R., Foley R. J., Li W., Swift B. J., Casebeer D., Filippenko A. V., 2006, AJ, 132, 189
Jordan G. C., IV, Perets H. B., Fisher R. T., van Rossum D. R., 2012, ApJ, 761, L23
Kromer M. et al., 2013, MNRAS, 429, 2287
Kromer M. et al., 2015, MNRAS, 450, 3045
Landolt A. U., 1992, AJ, 104, 340
Leibundgut B. et al., 1993, AJ, 105, 301
Li W. et al., 2003, PASP, 115, 453
Li W. et al., 2011, Nature, 480, 348
Liu Z.-W., Moriya T. J., Stancliffe R. J., Wang B., 2015a, A&A, 574, A12
Liu Z.-W., Stancliffe R. J., Abate C., Wang B., 2015b, ApJ, 808, 138
McClelland C. M. et al., 2010, ApJ, 720, 704
McCully C. et al., 2014a, Nature, 512, 54
McCully C. et al., 2014b, ApJ, 786, 134
Maeda K., Mazzali P. A., Deng J., Nomoto K., Yoshii Y., Tomita H., Kobayashi Y., 2003, ApJ, 593, 931
Marion G. H., Höflich P., Gerardy C. L., Vacca W. D., Wheeler J. C., Robinson E. L., 2009, AJ, 138, 727
Masi G. et al., 2014, Cen. Bur. Electron. Telegrams, 3949, 2
Moriya T., Tominaga N., Tanaka M., Nomoto K., Sauer D. N., Mazzali P. A., Maeda K., Suzuki T., 2010, ApJ, 719, 1445
Mould J. R. et al., 2000, ApJ, 529, 786
Narayan G. et al., 2011, ApJ, 731, L11
Nomoto K., Kamiya Y., Nakasato N., 2013, in Stefano R. D., Orio M., Maxwell M., eds, Proc. IAU Symp. 281, Binary Paths to Type Ia Supernovae Explosions. Cambridge Univ. Press, Cambridge, p. 253
Nugent P., Phillips M., Baron E., Branch D., Hauschildt P., 1995, ApJ, 455, L147
Nugent P., Baron E., Branch D., Fisher A., Hauschildt P. H., 1997, ApJ, 485, 812
Parrent J. T. et al., 2011, ApJ, 732, 30
Patat F., Benetti S., Cappellaro E., Danziger I. J., della Valle M., Mazzali P. A., Turatto M., 1996, MNRAS, 278, 111
Phillips M. M., 1993, ApJ, 413, L105
Phillips M. M. et al., 2007, PASP, 119, 360
Phillips M. M. et al., 2013, ApJ, 779, 38
Pinto P. A., Eastman R. G., Rogers T., 2001, ApJ, 551, 231
Piro A. L., Nakar E., 2014, ApJ, 784, 85
Poznanski D., Ganeshalingam M., Silverman J. M., Filippenko A. V., 2011, MNRAS, 415, L81
Poznanski D., Prochaska J. X., Bloom J. S., 2012, MNRAS, 426, 1465

Downloaded from https://academic.oup.com/mnras/article/459/1/1018/2609052 by CIS Psicologia Biblioteca F.Metelli - Universita degli Studi di Padova user on 30 September 2020

Puckett T., Gagliano R., Grcevich J., Storr J., Brissenden G., 2006, Cen. Bur. Electron. Telegrams, 625, 1
Riess A. G. et al., 1999, AJ, 118, 2675
Sahu D. K. et al., 2008, ApJ, 680, 580
Schlafly E. F., Finkbeiner D. P., 2011, ApJ, 737, 103
Schlegel D. J., Finkbeiner D. P., Davis M., 1998, ApJ, 500, 525
Stritzinger M., Leibundgut B., 2005, A&A, 431, 423
Stritzinger M. et al., 2002, AJ, 124, 2100
Stritzinger M., Leibundgut B., Walch S., Contardo G., 2006a, A&A, 450, 241
Stritzinger M., Mazzali P. A., Sollerman J., Benetti S., 2006b, A&A, 460, 793
Stritzinger M. D. et al., 2014, A&A, 561, A146
Stritzinger M. D. et al., 2015, A&A, 573, A2
Suntzeff N. B., 1996, in McCray R., Wang Z., eds, Proc. IAU Colloq. 145: Supernovae and Supernova Remnants. Cambridge Univ. Press, Cambridge, p. 41
Szalai T. et al., 2015, MNRAS, 453, 2103
Tomasella L. et al., 2014, Astron. Nachr., 335, 841
Tripp R., 1998, A&A, 331, 815
Tripp R., Branch D., 1999, ApJ, 525, 209
Turatto M., Benetti S., Cappellaro E., Danziger I. J., Della Valle M., Gouiffes C., Mazzali P. A., Patat F., 1996, MNRAS, 283, 1
Turatto M., Benetti S., Cappellaro E., 2003, in Hillebrandt W., Leibundgut B., eds, From Twilight to Highlight: The Physics of Supernovae. Springer-Verlag, Berlin, p. 200
Valenti S. et al., 2008, MNRAS, 383, 1485
Valenti S. et al., 2009, Nature, 459, 674
Wang B., Meng X., Liu D.-D., Liu Z.-W., Han Z., 2014, ApJ, 794, L28
Wheeler J. C., Johnson V., Clocchiatti A., 2015, MNRAS, 450, 1295
Yamanaka M. et al., 2015, ApJ, 806, 191

This paper has been typeset from a TEX/LATEX file prepared by the author.

Downloaded from https://academic.oup.com/mnras/article/459/1/1018/2609052 by CIS Psicologia Biblioteca F.Metelli - Universita degli Studi di Padova user on 30 September 2020